

AD-A110 844

DELAWARE UNIV NEWARK DEPT OF MECHANICAL AND AEROSPA--ETC F/6 20/4
TRANSONIC PRESSURE DISTRIBUTION AND BOUNDARY LAYER CHARACTERIST--ETC(U)
JUN 81 J E DANBERG, R H TSCHIRSCHNITZ DAA629-78-6-0057

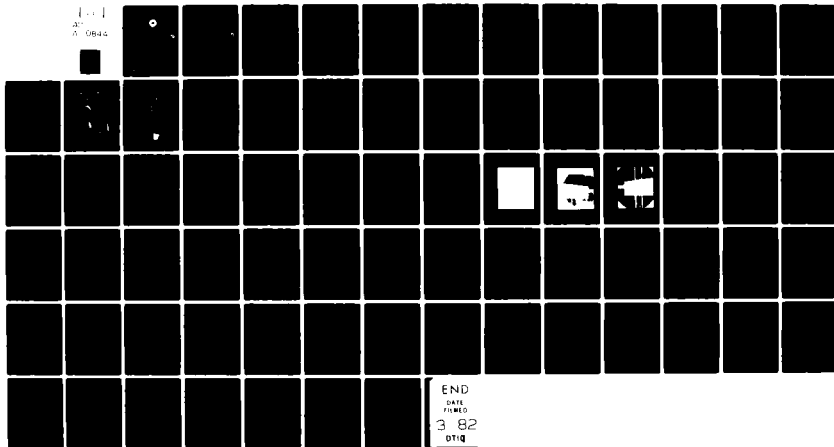
UNCLASSIFIED

TR-243

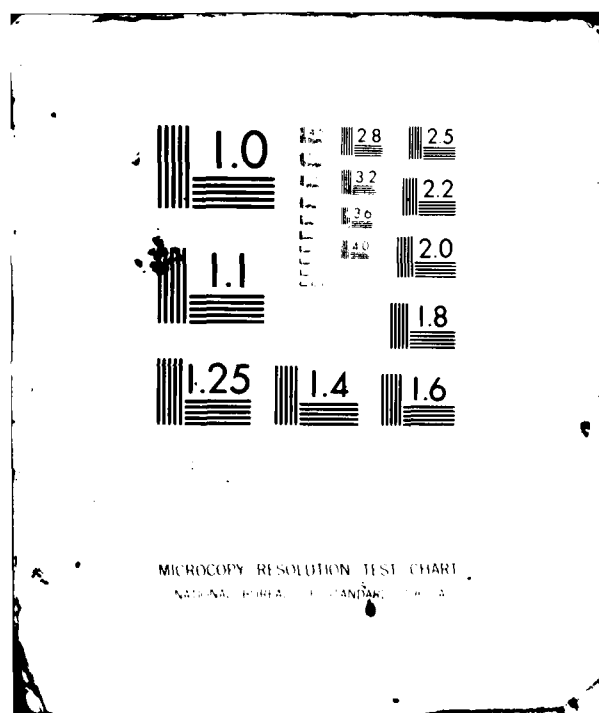
ARO-15172.4-E

NL

1-1
2-
A-0844



END
DATE
FILMED
3 82
DTIC



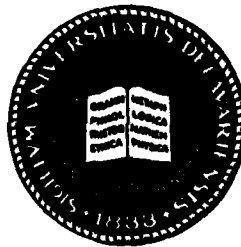
Technical Report No. 243

LEVEL II

ARO 15172.4-E

①

AD A110844



Transonic Pressure Distribution and
Boundary Layer Characteristics of a
Projectile With an Asymmetric Afterbody

Final Report

J. E. Danberg
R. H. Tschirschnitz

June 1981

U. S. Army Research Office

Contract DAAG29-78-G-0057

Department of Mechanical and Aerospace Engineering
University of Delaware
Newark, Delaware 19711

Approved for Public Release;
Distribution Unlimited.

DTIC FILE COPY

DTIC
SELECTED
FEB 10 1982
H

82 02 09 035

Transonic Pressure Distribution and
Boundary Layer Characteristics of a
Projectile With an Asymmetric Afterbody

Final Report

J. E. Danberg
R. H. Tschirschnitz

June 1981

U. S. Army Research Office

Contract DAAG29-78-G-0057

Department of Mechanical and Aerospace Engineering
University of Delaware
Newark, Delaware 19711

Approved for Public Release;
Distribution Unlimited.

DTIC
SELECTED
FEB 10 1982
H

UNCLASSIFIED

SECURITY CLASSIFICATION OF THIS PAGE (When Data Entered)

REPORT DOCUMENTATION PAGE		READ INSTRUCTIONS BEFORE COMPLETING FORM
1. REPORT NUMBER	2. GOVT ACCESSION NO. AD-A110844	3. RECIPIENT'S CATALOG NUMBER
4. TITLE (and Subtitle) TRANSONIC PRESSURE DISTRIBUTION AND BOUNDARY LAYER CHARACTERISTICS OF A PROJECTILE WITH AN ASYMMETRIC AFTERBODY.		5. TYPE OF REPORT & PERIOD COVERED Final Report Feb. 1978-June 1981
		6. PERFORMING ORG. REPORT NUMBER Univ. of Delaware Tech. Report No.
7. AUTHOR(s) J. E. Danberg R. H. Tschirschnitz		8. CONTRACT OR GRANT NUMBER(s) 6 DAAG29-78-6-0057
9. PERFORMING ORGANIZATION NAME AND ADDRESS Mechanical and Aerospace Engineering Department, University of Delaware, Newark, Delaware 19711		10. PROGRAM ELEMENT, PROJECT, TASK AREA & WORK UNIT NUMBERS
11. CONTROLLING OFFICE NAME AND ADDRESS U. S. Army Research Office Post Office Box 12211 Research Triangle Park, NC 27709		12. REPORT DATE June 1981
		13. NUMBER OF PAGES
14. MONITORING AGENCY NAME & ADDRESS (if different from Controlling Office)		15. SECURITY CLASS. (of this report) Unclassified
		15a. DECLASSIFICATION/DOWNGRADING SCHEDULE
16. DISTRIBUTION STATEMENT (of this Report) Approved for public release; distribution unlimited.		
17. DISTRIBUTION STATEMENT (of the abstract entered in Block 20, if different from Report) NA		
18. SUPPLEMENTARY NOTES The view, opinions, and/or findings contained in this report are those of the author(s) and should not be construed as an official Department of the Army position, policy, or decision, unless so designated by other documentation.		
19. KEY WORDS (Continue on reverse side if necessary and identify by block number) Projectile aerodynamics, transonic flow, boundary layers, asymmetric afterbody, boundary layer probing		
20. ABSTRACT (Continue on reverse side if necessary and identify by block number) TRANSONIC PRESSURE DISTRIBUTION AND BOUNDARY LAYER CHARACTERISTICS OF A PROJECTILE WITH AN ASYMMETRIC AFTERBODY <u>Abstract</u> Measurements of pressure distribution and boundary layer characteristics were obtained on an asymmetric boattail projectile. Such configurations are		

DD FORM 1 JAN 75 1473

EDITION OF 1 NOV 65 IS OBSOLETE

UNCLASSIFIED

SECURITY CLASSIFICATION OF THIS PAGE (When Data Entered)

being studied as potential alternatives to conventional boattails because of their reduced variation in moments in the transonic speed range.

Wind tunnel tests were performed in the NASA Langley Research Center 8' Transonic Pressure Tunnel on a 5.8 caliber model with a triangular, conical and cylindrical afterbody. Pressure distributions were attained at $M_\infty = 0.9, 0.94$ and 0.97 and at $\alpha = 0^\circ$ and 4° . An internally mounted probe mechanism was used to measure the three-dimensional boundary layer characteristics $M_\infty = 0.94$.

Integration of the pressure distribution data showed that the contribution of the triangular afterbody to the total drag is fifty percent of that of a conical configuration. Base drag and forebody drag for the triangular afterbody are assumed the same as for the conical boattail if the base areas are the same in the two cases. Integration of the moments of the pressure distribution permit the evaluation of the pitching moment contribution of the different afterbodies. The moments due to the triangular afterbody contribute relatively little to the overall pitching moment as compared to the strongly destabilizing effect of the conical boattail and the stabilizing effect of a cylindrical afterbody. Because of the asymmetric configuration the moments created depend on the orientation of the afterbody.

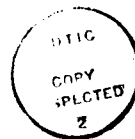
FOREWORD

This report summarizes the experimental research carried out under contract

DAAG29-78-G-0057

sponsored by the U.S. Army Research Office, Durham, N.C. Several University of Delaware undergraduate students contributed to the project including J. Kegelman (BME 1979) and Eric L. Kruger (BME 1980) who participated in the design and testing of the model and instrumentation. Mr. Kruger's senior research report was based on the asymmetric afterbody tests. Three other students participated in the data reduction and analysis and based their senior research on this project. They are: Carol Schubert (BME 1979) and John Thackrah (BME 1979) and George C. Bange (BME 1980).

The authors would like to express their appreciation for the help and guidance of Mr. Anders Platou of the U.S. Army, Ballistic Research Laboratory ARRADCOM and to the many others in BRL and the NASA Langley Research Center who contributed to the success of the project.



Accession For	
NTIS GRA&I	<input checked="checked" type="checkbox"/>
DTIC TAB	<input type="checkbox"/>
Unannounced	<input type="checkbox"/>
Justification	
By _____	
Distribution/	
Availability Codes	
Dist	Avail and/or Special
A	

TABLE OF CONTENTS

List of Illustrations

1. INTRODUCTION
2. EXPERIMENT
 1. Facility
 2. Model
 3. Instrumentation - Pressure Distribution
 4. Instrumentation - Boundary Layer Probe
 5. Instrumentation - Miscellaneous
3. RESULT - ZERO ANGLE OF ATTACK
 1. Zero Angle of Attack - Pressure Distribution
 2. Zero Angle of Attack - Mach Number Effects
 3. Comparison Between Triangular Conical and Cylindrical Afterbody Pressure Distributions
 4. Zero Angle of Attack - Boundary Layer Profiles
4. RESULTS - ANGLE OF ATTACK
 1. Circumferential Pressure Distribution
 2. Boundary Layer Characteristics
5. DISCUSSION
 1. Conical Boattail Results
 2. Boattail Drag
 3. Pitching Moment
6. SUMMARY AND CONCLUSIONS
7. REFERENCES.
8. LIST OF SYMBOLS.

LIST OF ILLUSTRATIONS

1. General arrangement of the NASA Langley Research Center transonic pressure tunnel.
2. Test section of the NASA Langley Research Center 8' transonic pressure tunnel.
3. Dimensions of triangular afterbody model.
4. Location of wall static pressure taps triangular afterbody model.
5. Test configurations of the model.
6. Boundary layer survey mechanism.
7. Sketch of three probe rake installed on the triangular afterbody model.
8. Nomenclature for defining probe dimensions.
9. Longitudinal pressure distribution at $M = 0.94$ triangular afterbody model.
10. Circumferential pressure distribution at $M = 0.94$, $x/L = 0.881$ triangular afterbody model.
11. Circumferential pressure distribution at $M = 0.94$ all x/L stations, triangular afterbody model.
12. Effect of Mach number on the longitudinal pressure distribution.
13. Schlieren photograph of afterbody flow field $\alpha=0^\circ$, $\phi=0^\circ$, $M=0.90$.
14. Schlieren photograph of afterbody flow field $\alpha=0^\circ$, $\phi=0^\circ$, $M=0.94$.
15. Schlieren photograph of afterbody flow field $\alpha=0^\circ$, $\phi=0^\circ$, $M=0.97$.
16. Comparison between pressure distribution measured on conical, cylindrical and triangular afterbodies.
17. Comparison between rake probe and single probe boundary layer velocity profiles.
18. Velocity profiles at $x/L = 0.881$, $\alpha = 0^\circ$, $M = 0.94$.
19. Centerline velocity profiles at two longitudinal stations, $x/L = 0.881$ and 0.924 , $\alpha = 0^\circ$, $M = 0.94$.

20. Total boundary layer thickness as a function of circumferential position at $x/L = 0.881$, $\alpha = 0^\circ$, $M = 0.94$.
21. Circumferential distribution of pressure coefficients on triangular afterbody in Orientation A for five longitudinal stations ($M_\infty = 0.94$, $\alpha = 4^\circ$).
22. Circumferential distribution of pressure coefficients on triangular afterbody in Orientation B for five longitudinal stations ($M_\infty = 0.94$, $\alpha = 4^\circ$).
23. Circumferential distribution of boundary layer thickness on triangular afterbody in Orientation A ($M_\infty = 0.94$, $\alpha = 4^\circ$, $x/L = 0.881$).
24. Circumferential distribution of boundary layer thickness on triangular afterbody in Orientation B ($M_\infty = 0.94$, $\alpha = 4^\circ$, $x/L = 0.881$).
25. Pitching moment coefficient slope vs. Mach number for several afterbody configurations (Ref. 12).
26. Zero angle of attack drag coefficient for several afterbody configurations (Ref. 12).
27. Conical boattail model configuration showing dimensions.
28. Effect of Mach number on zero angle of attack pressure distribution for the conical boattail model.
29. Pressure coefficient distribution on conical boattail, $\alpha = 4^\circ$, $M_\infty = 0.80$.
30. Pressure coefficient distribution on conical boattail, $\alpha = 4^\circ$, $M_\infty = 0.94$.
31. Pressure coefficient distribution on conical boattail, $\alpha = 4^\circ$, $M_\infty = 0.97$.
32. Boattail contribution to the drag coefficient for a conical and triangular configuration.
33. Afterbody contribution to the pitching moment coefficient - cylindrical afterbody ($M_\infty = 0.94$, $\alpha = 4^\circ$).
34. Afterbody contribution to the pitching moment coefficient - 7° conical boattail ($M_\infty = 0.94$, $\alpha = 4^\circ$).
35. Afterbody contribution to the pitching moment coefficient - triangular boattail ($M_\infty = 0.94$, $\alpha = 4^\circ$).

INTRODUCTION

Modern artillery must be capable of delivering projectiles over a wide range of conditions from long range, high velocity to high elevation and relatively low velocity. The low velocity situation is one of the most critical because under these conditions the projectile passes through the transonic speed range. At transonic speeds the aerodynamic characteristics of the projectile experience wide variations. Pitching and magnus moment variations are particularly important because of their negative effects on gyroscopic stability and thus accuracy.

Low pressure supersonic regions generated at transonic speeds by surface discontinuities and their termination by shock waves leads to asymmetric negative lift forces on the projectile at angle of attack. Boattail configurations introduced to reduce base drag produces expansion regions at the boattail junction. At small angles of attack, the center of pressure of the lift is substantially forward of the center of gravity producing large positive or distabilizing moments. The extent of the low pressure region on the afterbody is sensitive to Mach number because the shock wave location is a strong function of Mach number. The consequences of the strongly varying flow field are equally strong and unfavorable effects on stability.

It is desirable to consider unconventional boattail configurations in an attempt to reduce the Mach number effects on forces and moments while retaining the low drag properties of the normal conical boattail. A. Platou at the U. S. Army Ballistic Research Laboratory initiated several wind tunnel and ballistic range studies of unconventional configurations in the early 1970's. These studies lead to the conclusion that boattail configurations formed by cutting the main projectile cylinder with planes inclined at a shallow angle such that fin-like surfaces are formed on the boattail favorably effected the moments. One of the most successful configurations uses three planes so as to form an inscribed triangle at the base (triangular boattail). The planes can be canted

or twisted consistent with the gun rifling to reduce flow interference at design spin rates. Measured drag on this configuration has been found to be comparable or lower than that of conical afterbody projectiles if the base areas are the same, whereas the pitching moment coefficients are significantly reduced.¹⁻⁴ Transonic Magnus moments are also found to be less severe. In addition to the aerodynamic advantages these projectiles can also have better internal volume distribution and thus provide the designer with more control over center of gravity location. Test firings^{5,6} of full scale 105 and 155 mm projectiles have also been carried out to demonstrate the practicality of these configurations.

The objective of the present study is to obtain detailed pressure distributions and boundary layer data on projectile models with triangular boattails at transonic speeds with the ultimate purpose of securing a better understanding of the flow fields which produce the advantageous effects observed in force balance and free flight tests. Such improved understanding may be expected to

¹A. S. Platou. "An Improved Projectile Boattail," AIAA Paper No. 74-779, AIAA Mechanics and Control of Flight Conference, 1974.

²A. S. Platou. "An Improved Projectile Boattail," BRL Memorandum Report No. 2395, U. S. Army Ballistic Research Laboratories, Aberdeen Proving Ground, MD, 1974.

³A. S. Platou. "An Improved Projectile Boattail, Part II," BRL Report No. 1866, U. S. Army Ballistic Research Laboratories, Aberdeen Proving Ground, MD, 1976.

⁴A. S. Platou. "An Improved Projectile Boattail, Part III," BRL Memorandum Report No. 2644, U. S. Army Ballistic Research Laboratories, Aberdeen Proving Ground, MD, 1976.

⁵A. S. Platou. "Yawsonde Flights of 155 MM Non-Conical Boattail Projectiles and the 155 MM Projectile at Tonapah Test Range - October 1977," BRL Memorandum Report ARB2L-MR-02881, U. S. Army Armament Research and Development Command, Ballistic Research Laboratory, Aberdeen Proving Ground, MD, 1978.

⁶A. S. Platou. "Yawsonde Flights of 155 MM Non-Conical Boattail Projectile - B Configurations at Tonopah Test Range - March 1978," U. S. Army Ballistic Research Laboratory ARADCOM Memorandum Report ARBRL-MR-02908, Aberdeen Proving Ground, MD, 1979.

lead to improved designs.

A secondary objective is to provide bench mark data on a complex three-dimensional transonic flow field which may be used to test three-dimensional computational methods currently under development.

Deiwert⁷ has recently described a powerful numerical technique capable of handling the three-dimensional flow field about axisymmetric afterbodies at angle of attack and applicable at transonic speeds. In this work he has shown good ability to describe the expansion and compression flow fields on the afterbody when compared to the results of several experimental studies⁸⁻¹⁰ of axisymmetric boattail characteristics. These solutions to the Navier-Stokes equation based on the work of Pulliam and Steger¹¹ and Scheff and Steger¹² are potentially capable of including the nonsymmetric body geometry.

As a first step in approaching the above objectives measurements were obtained on a conventional boattail model (7° conical)

⁷G. S. Deiwert. "Numerical Simulation of Three-Dimensional Boattail Afterbody Flow Fields," AIAA Journal 19, 5, pp. 582-588, 1981.

⁸D. E. Reubush. "Experimental Study of the Effectiveness of Cylindrical Plume Simulators for Predicting Jet-On Boattail Drag at Mach Numbers up to 1.30," NASA TN D-7795, 1974.

⁹J. A. Benek. "Separated and Non-Separated Turbulent Flows About Axisymmetric Nozzle Afterbodies, Part I, Detailed Surface Measurement," AEDC-TR-78-79; Part II, Detailed Flow Measurement," AEDC-TR-79-22, October 1979.

¹⁰G. D. Shrewsbury. "Effect of Boattail Junction Shape on Pressure Drag Coefficients of Isolated Afterbodies," NASA TNX-1517, 1968.

¹¹T. H. Pulliam and J. L. Steger. "On Implicit Finite Difference Simulation of Three Dimensional Flow," AIAA Journal 18, 2, pp. 159-167, 1980.

¹²L. B. Scheff and J. L. Steger. "Numerical Simulation of Steady Supersonic Viscous Flow," AIAA Paper No. 79-130, New Orleans, LA, 1979.

which has been reported on elsewhere.^{13,14} In addition other pressure distribution tests at transonic speeds on an asymmetric boattail configuration were reported by Kayser and Sturek.¹⁵

¹³J. E. Danberg, R. P. Reklis and G. R. Inger. "Pressure Distributions and Boundary Layer Profiles on a Yawed Projectile at Transonic Speeds," Technical Report #226, Department of Mechanical and Aerospace Engineering, University of Delaware, Newark, DE, 1979.

¹⁴R. P. Reklis, J. E. Danberg and G. R. Inger. "Boundary Layer Flows on Transonic Projectiles," AIAA Paper No. 79-1551, AIAA 12th Fluid and Plasma Dynamics Conference, Williamsburg, VA, 1979.

¹⁵L. D. Kayser and W. B. Sturek. "Aerodynamics Performance of Projectiles with Axisymmetric and Non-Axisymmetric Boattails," Memorandum Report No. 03022, U. S. Army Armament Research and Development Command, Ballistic Research Laboratory, Aberdeen Proving Ground, MD, 1980.

EXPERIMENT

Facility

The experiment reported here was performed in the NASA Langley Research Center 8 foot Transonic Pressure Tunnel (TPT). A general arrangement and sketch of the tunnel is shown in Figure 1. For the test of the triangular boattail model, the tunnel was operated at one atmosphere supply pressure (101.3 kPa) and at a supply temperature of 49.2°C which resulted in a Reynolds number of 13×10^6 per meter. The TPT is of slotted wall construction, as illustrated in Figure 2, to minimize reflected wave interference effects. The interference of the model on the tunnel flow was monitored using tunnel wall static pressure taps. The model was sting mounted from the NASA support sector and roll mechanism which allowed measurements at angle of attack and in various roll positions.

The pressure distributions data reported here were obtained at three tunnel Mach numbers 0.90, 0.94 and 0.97 and at two angles of attack 0° and 4°. Boundary layer surveys were made only at $M = 0.94$ but covered several orientations of the model at $\alpha = 0^\circ$ and 4°.

Model

The main components of the model were furnished by the U. S. Army Ballistic Research Laboratory and corresponded approximately to a typical modern artillery projectile as shown in Figure 3.

A major modification concerned the afterbody which was originally designed with a one caliber conical boattail of 7°. For these tests a nonconical boattail was manufactured in which three flat surfaces were arranged on the model afterbody inclined at 7° to the model centerline. These surfaces would culminate in an inscribed triangular cross section in 2 calibers. The afterbody was truncated after 1.446 calibers because of instrumentation limitations. In applications of the nonconical afterbody to ar-

NASA
L-70-5601

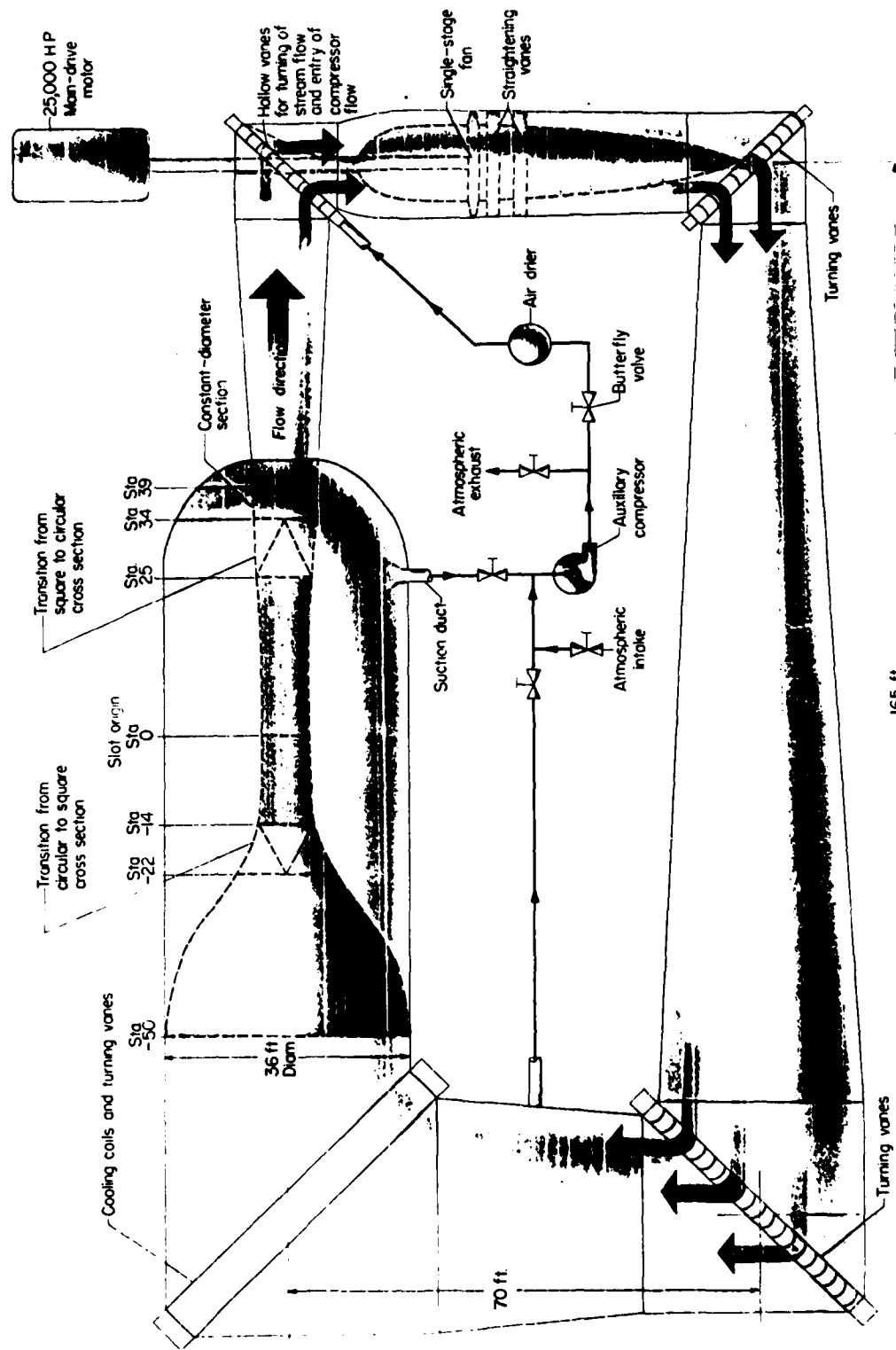


Figure 1. General arrangement of the NASA Langley Research Center transonic pressure tunnel.

NASA
L-79-5316

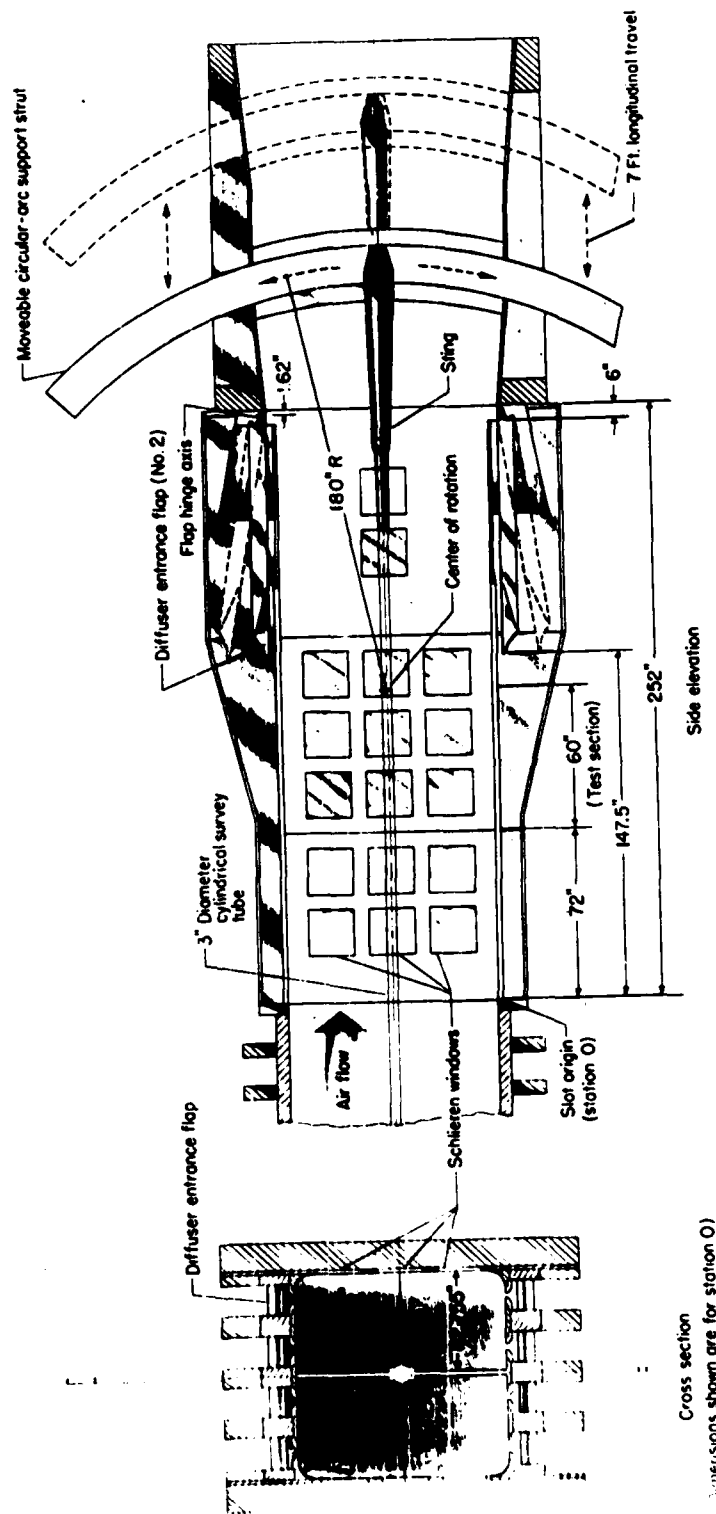


Figure 2. Test section of the NASA Langley Research Center 8' transonic pressure tunnel.

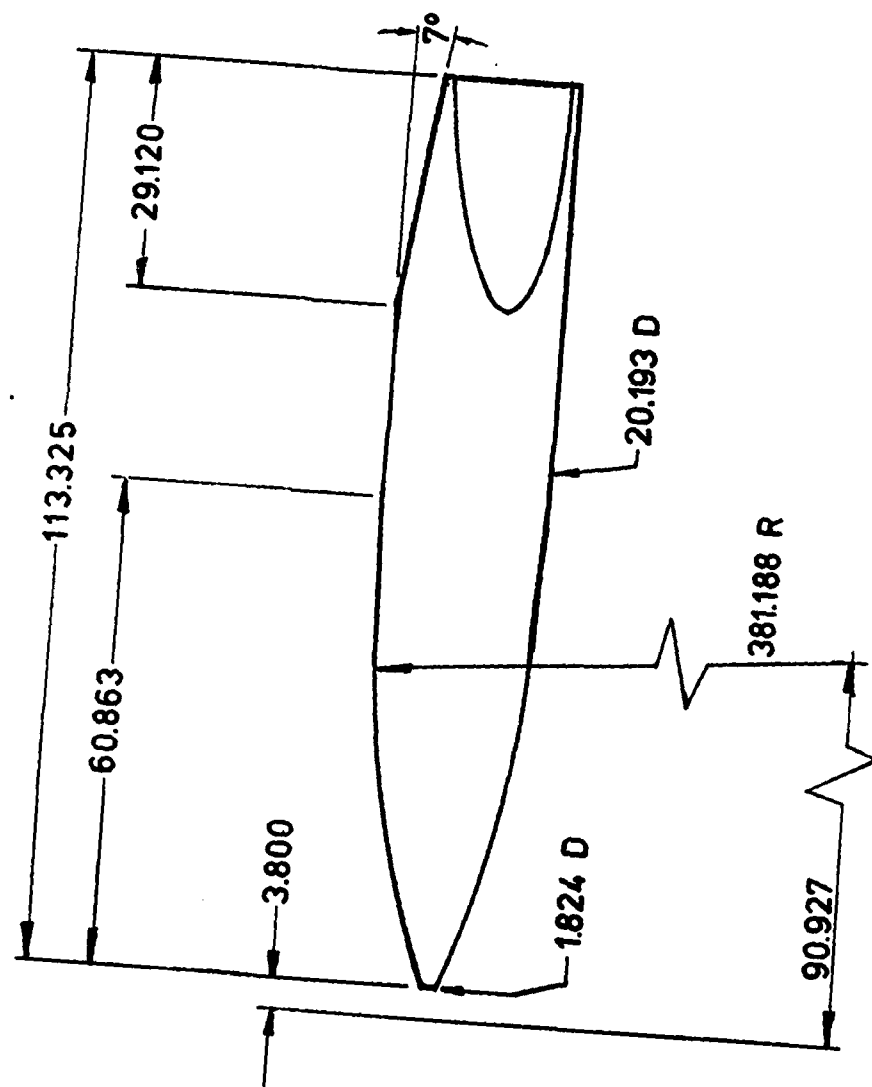


Figure 3. Dimensions of triangular afterbody model.

tillery projectiles the boattail would probably be geometrically twisted to reduce flow interference because of spin. Since these wind tunnel tests were limited to the nonspinning situation by the probing technique, a straight afterbody more nearly represents the correct flow pattern.

Uniform transition to turbulent flow was assured by using a carborundum grain roughness strip 5 cm from the nose. The 20.2 cm diameter model caused 0.69% blockage of the tunnel which was believed acceptable for the kinds of measurements carried out.

Instrumentation-Pressure Distribution

A total of 31 surface pressure orifices were installed over both the flat and cylindrical portions of the boattail as shown in Figure 4 and their locations are defined in Table 1. Pressure taps were located only in the afterbody region because the basic model internal configuration was designed to accommodate force balance instrumentation and an air turbine to spin the outer shell. Major structural changes would have been required to instrument the forebody. The pressure taps were arranged unsymmetrically on the flat surface so that at angles of attack more distribution data could be obtained by taking advantage of the model symmetry in roll.

Because of the asymmetry of the model, the pressure distribution at angle of attack is a function of the roll angle. Representative roll orientations were investigated and may be characterized in terms of the orientation of the instrumented surfaces relative to the cross flow. Four configurations were considered as shown in Figure 5. Primary interest was focused on configuration A and B and because of the symmetry in the cross flow plane. Measurements were taken at $\alpha = \pm 4^\circ$ and $\phi = \pm 60^\circ$ but for purposes of presentation the data are associated with the appropriate surface as would be observed at $\alpha = + 4^\circ$ and either 0° , 30° or 60° of roll. The actual model orientations in which measurements were made are related to the three configurations in Figure 5.

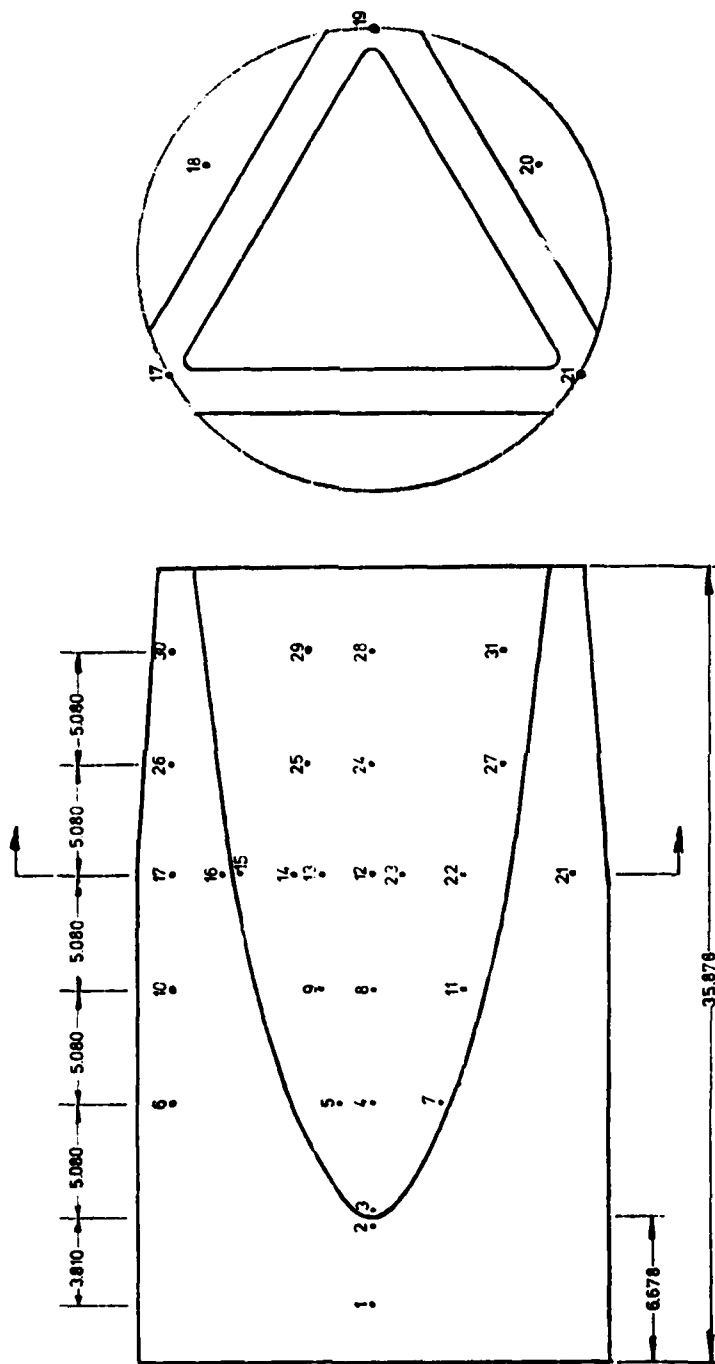


Figure 4. Location of wall static pressure taps triangular afterbody model.

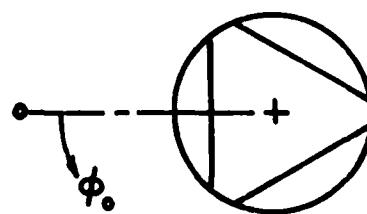
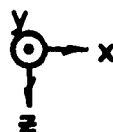
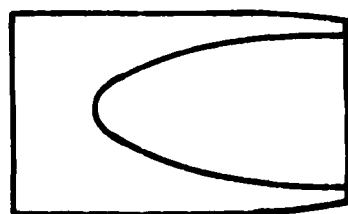
TABLE 1
WALL STATIC PRESSURE TAP LOCATIONS
(TRIANGULAR AFTERBODY)

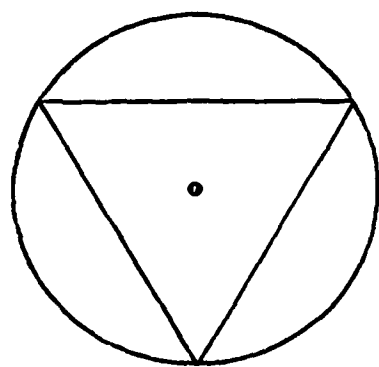
TAP	X (m)	X/L	Z (cm)	Z/D	ϕ_o (deg.)
1	.85385	.72901	0.0	0.0	0
2	.87632	.74820	0.0	0.0	0
3	.88217	.75319	0.0	0.0	0
4	.93005	.79407	0.0	0.0	0
5	.93005	.79407	-1.37	-0.06792	- 8.239
6	.93005	.79407	-	-	- 60
7	.93005	.79407	2.77	0.13711	16.292
8	.98085	.83744	0.0	0.0	0
9	.98085	.83744	-2.11	-0.10440	- 13.400
10	.98085	.83744	-	-	- 60
11	.98085	.83744	3.81	0.18868	23.295
12	1.03165	.88081	0.0	0.0	0
13	1.03165	.88081	-2.11	-0.10440	14.376
14	1.03165	.88081	-3.51	-0.17358	23.081
15	1.03165	.88081	-5.55	-0.27484	34.009
16	1.03165	.88081	-	-	- 36.714
17	1.03165	.88081	-	-	- 60
18	1.03165	.88081	-	-	-120
19	1.03165	.88081	-	-	180
20	1.03165	.88081	-	-	120
21	1.03165	.88081	-	-	60
22	1.03165	.88081	3.81	0.18868	24.954
23	1.03165	.88081	1.17	0.05786	8.085
24	1.08245	.92418	0.0	0.0	0
25	1.08245	.92418	-2.77	-0.13711	- 20.012
26	1.08245	.92418	-	-	- 60
27	1.08245	.92418	5.55	0.27547	36.196
28	1.13325	.96756	0.0	0.0	0
29	1.13325	.96756	2.77	0.13711	- 21.642
30	1.13325	.96756	-	-	- 60
31	1.13325	.96756	5.55	0.27547	38.561

X = Measured from datum

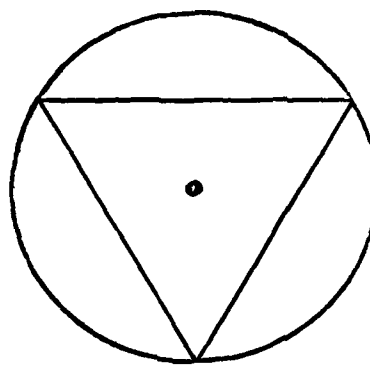
D = 20.193 cm

L = 1.1712 m

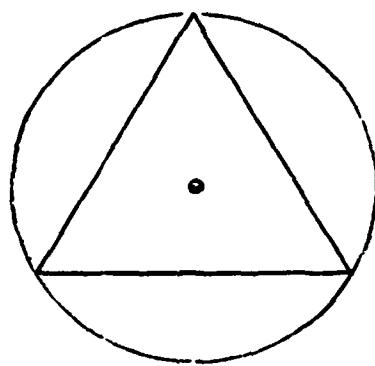




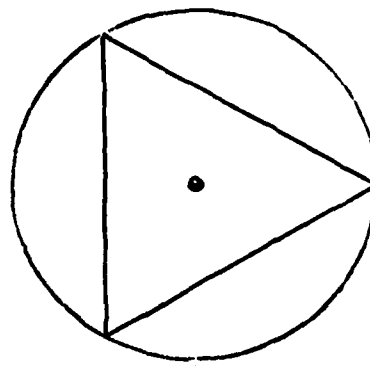
CONFIGURATION 0
 $\alpha = 0^\circ$ $\phi = 0^\circ$



CROSSFLOW
 CONFIGURATION A
 $\alpha = +4^\circ$ $\phi = 0^\circ$



CROSSFLOW
 CONFIGURATION B
 $\alpha = +4^\circ$ $\phi = 60^\circ$



CROSSFLOW
 CONFIGURATION C
 $\alpha = +4^\circ$ $\phi = 30^\circ$

Figure 5. Test configurations of the model.

In that table ϕ is the angle between the normal to the instrumented surface and the lee side of the model.

The pressure orifices were connected via flexible tubing to an internally mounted Scani valve which connected any tap location to a 0 - 35 kPa transducer (of 0.25% full scale accuracy) on signal from the control room. The surface pressures were measured relative to the tunnel static pressure which was monitored continuously by the normal tunnel instrumentation.

Instrumentation-Boundary Layer Probe

The model afterbody contains an internally mounted boundary layer survey mechanism used in previous tests^{1,2,3} as shown in Figure 6 installed in a conical afterbody model. Some minor changes in positioning of components were required because of the more restrictive base configuration of the triangular afterbody but the basic operation of the system was unaffected. The probe travel was controlled by a D.C. electric motor driving a micrometer lead screw. The speed control allowed positioning within ± 0.1 mm. The probe tip was electronically insulated so that wall contact provides a reference position for calibration in the tunnel.

Two kinds of probes were constructed for use with the triangular afterbody; one consisted of a three probe rake which was designed to survey the boundary layer at three lateral station simultaneously. The other was a conventional, minimum interference, simple probe configuration similar to those used in earlier investigations on the conical afterbody. Interference effects created by the rake were of major concern and therefore where possible the rake data was duplicated using the single probe. On the cylindrical sections of the boattail, however, only the single probe could be used.

Figure 7 shows the general arrangement of the three probe rake and Figure 8 defines the nomenclature used to describe the probe and supporting arm geometry. Table 2 defines the probe con-

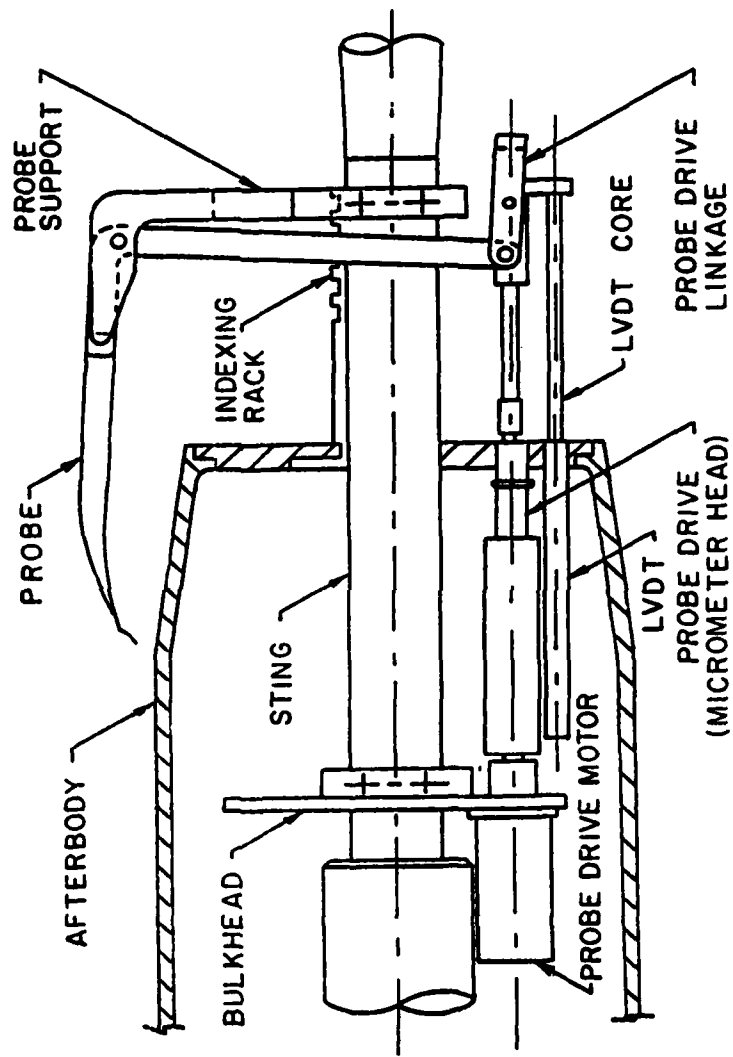


Fig. 6 Boundary layer survey mechanism

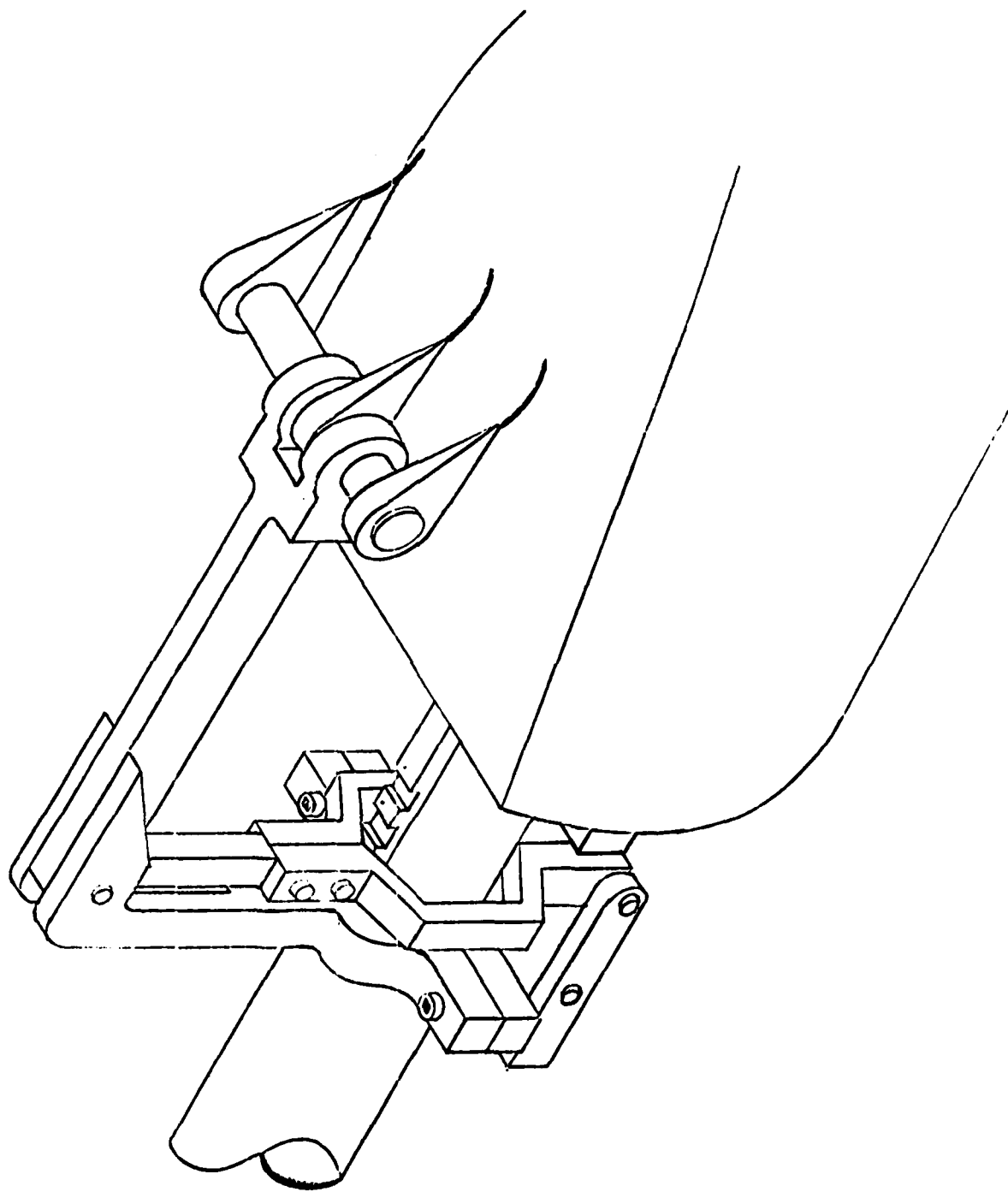


Figure 7. Sketch of three probe rake installed on the triangular afterbody model.

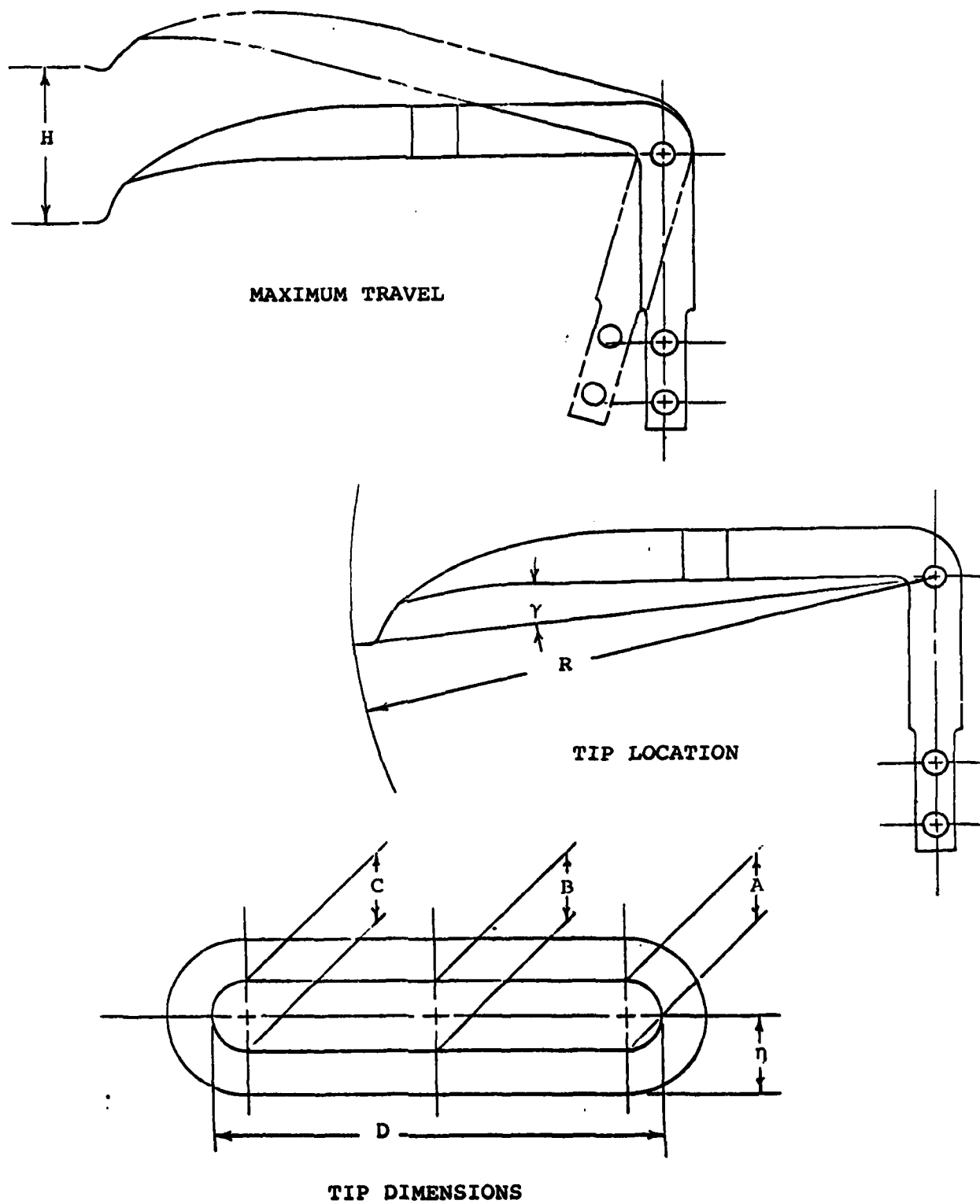


Fig. 8 Nomenclature for defining probe dimensions

TABLE 2
PROB. CONFIGURATION DATA

<u>PROBE DESIGNATION</u>	η (mm)	\underline{D} (mm)	\underline{C} (mm)	\underline{B} (mm)	\underline{A} (mm)
1/2" CONICAL	1.80×10^{-1}	1.08	1.25×10^{-1}	1.34×10^{-1}	1.26×10^{-1}
1-1/2" CONICAL	2.01×10^{-1}	1.06	1.32×10^{-1}	1.21×10^{-1}	1.16×10^{-1}
2-1/2" CONICAL	1.85×10^{-1}	1.04	9.40×10^{-2}	1.12×10^{-1}	1.12×10^{-1}
3-1/2" CONICAL	1.85×10^{-1}	1.04	9.40×10^{-2}	1.12×10^{-1}	1.12×10^{-1}
4-1/2" CONICAL	1.65×10^{-1}	1.33	1.45×10^{-1}	1.28×10^{-1}	1.31×10^{-1}
6" CONICAL	1.65×10^{-1}	1.33	1.45×10^{-1}	1.28×10^{-1}	1.34×10^{-1}
(#1) TRIANGULAR (FLATSIDE)	1.72×10^{-1}	1.10	1.27×10^{-1}	1.07×10^{-1}	1.34×10^{-1}
(#2) TRIANGULAR (FLATSIDE)	1.92×10^{-1}	1.10	1.08×10^{-1}	1.15×10^{-1}	1.25×10^{-1}
(#3) TRIANGULAR (FLATSIDE)	1.73×10^{-1}	9.87×10^{-1}	1.37×10^{-1}	1.31×10^{-1}	1.35×10^{-1}
1-1/2" TRIANGULAR (CYLINDRICAL SIDE)	1.36×10^{-1}	1.28	1.10×10^{-1}	1.23×10^{-1}	1.10×10^{-1}
3-1/2" TRIANGULAR (CYLINDRICAL SIDE)	1.38×10^{-1}	1.25	1.01×10^{-1}	1.09×10^{-1}	9.65×10^{-2}
5-1/2" TRIANGULAR (CYLINDRICAL SIDE)	1.38×10^{-1}	1.25	1.01×10^{-1}	1.09×10^{-1}	9.65×10^{-2}

TABLE 2 (Cont.)

<u>PROBE DESIGNATION</u>	<u>R(cm)</u>	<u>$\gamma(^{\circ})$</u>
1/2" CONICAL	11.93	12.5
1 1/2" CONICAL	14.35	9.5
2 1/2" CONICAL	16.79	6.8
3 1/2" CONICAL	16.79	6.8
4 1/2" CONICAL	20.52	4.4
6" CONICAL	20.52	4.4
1 1/2" TRIANGULAR (CYLINDRICAL SIDE)	11.67	
3 1/2" TRIANGULAR (CYLINDRICAL SIDE)	19.21	5.0
5 1/2" TRIANGULAR (CYLINDRICAL SIDE)	19.21	5.0

figuration. Probe half heights (η) varied from 0.2 to 0.14 mm which defined the point closest to the model surface.

The total head pressures detected by the probes were measured on a 0 to 70 kPa differential transducer with the reference pressure equal to the tunnel supply pressure.

Instrumentation-Miscellaneous

The model angle of attack was monitored using a Kearfott accelerometer mounted on a bulkhead inside the model. Although the instrument was calibrated statically in the tunnel with the model at zero roll ($\phi = 0^\circ$), the instrument could not simultaneously be calibrated in the various roll positions employed. Thus, the angle of attack was established at $\phi = 0^\circ$ and the model rolled to the test conditions.

Schlieren photographs of the model and its shock wave system were obtained at selected points throughout the tests.

RESULTS - ZERO ANGLE OF ATTACK

The discussion of results is naturally divided into two main sections; the first having to do with $\alpha=0^\circ$ results and the second dealing with angle of attack effects. Within each section there is consideration of pressure distributions and boundary layer survey data. Although the pressure measurements are limited to the afterbody regime it is not expected that the afterbody configuration would have much effect on the forebody pressure distribution except just ahead of the junction with the afterbody.

Zero Angle of Attack - Pressure Distribution

The asymmetric nature of the model implies that the pressure distribution is a function of both the circumferential and longitudinal station even in the zero angle of attack case.

The longitudinal pressure distribution at $M=0.94$ is shown in Figure 9 where the pressure coefficient defined as:

$$C_p = (p - p_\infty) / q_\infty$$

is plotted versus longitudinal position as a fraction of total body length. Two distributions are shown; one for the centerline of the flat surface and the other for the mid-point on the cylindrical section between the flats. Note that there are two taps, one on the forebody 1.27cm ahead of the flat and a second located 1.27cm downstream of the juncture. This figure shows the sharp expansion peak or low pressure created as the flow turns from the cylindrical section to the flat. As a point of reference, the minimum pressure coefficient calculated for a Prandtl Mayer expansion of 7° starting from sonic velocity gives $C_p = -0.49$ compared to the measured C_p of -0.4 . Viscous displacement effects are expected to reduce the effective turning angle and thereby reduce the calculated pressure coefficient.

The pressure coefficient increases rather rapidly following

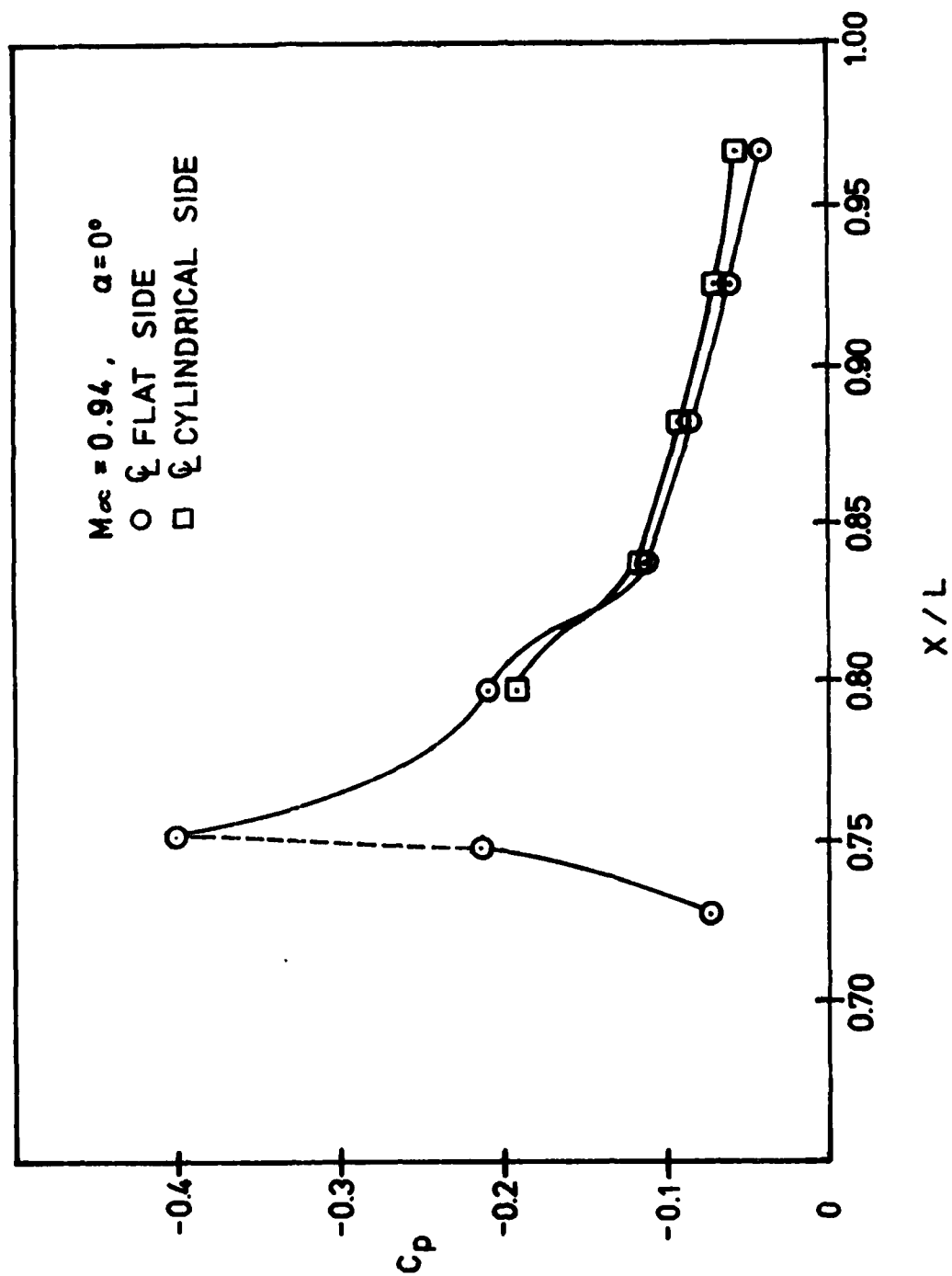


Figure 9. Longitudinal pressure distribution at $M = 0.94$ triangular afterbody model.

the afterbody junction and levels off about 0.6 a caliber ($\Delta x/L \approx 0.1$) downstream, following which there is a slow but steady approach to the pressure conditions that existed on the cylinder ahead of the afterbody. The last pressure on the centerline of the flat is less than 1% lower than the measured base pressure, the effects of which may be expected to be felt a short distance upstream of the base.

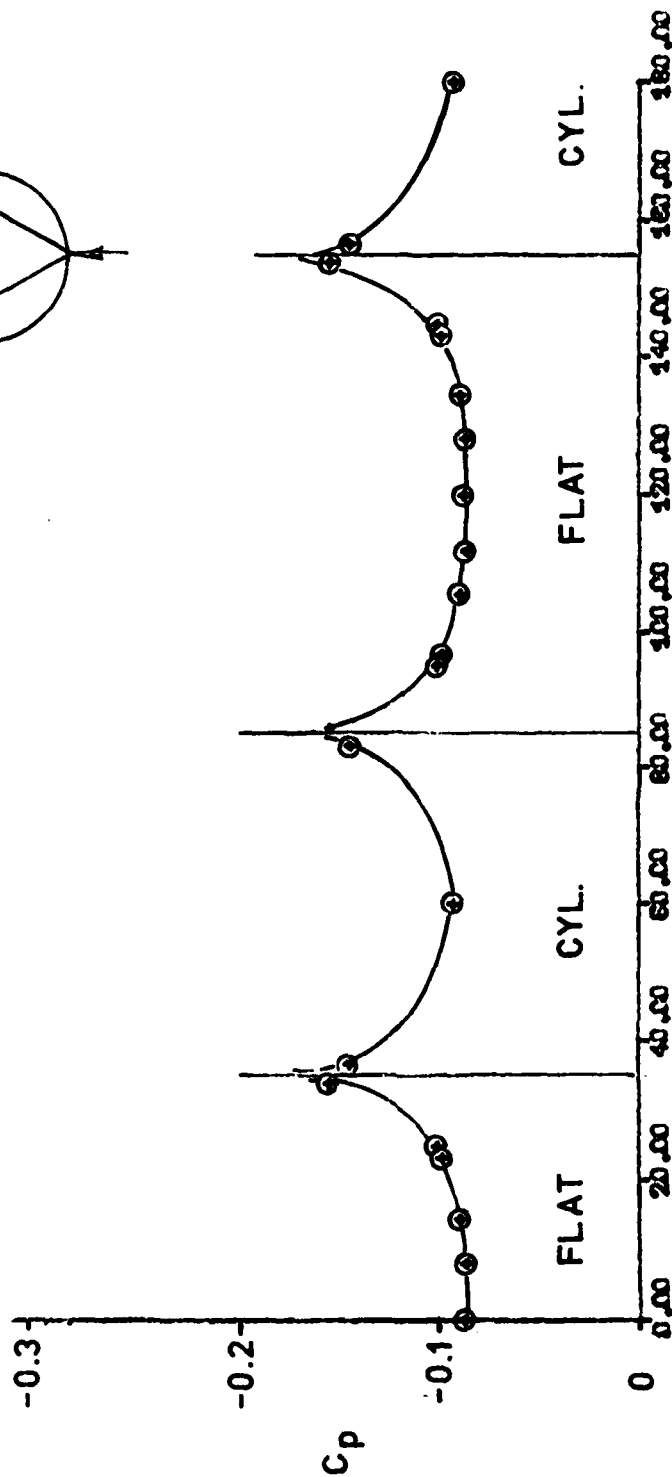
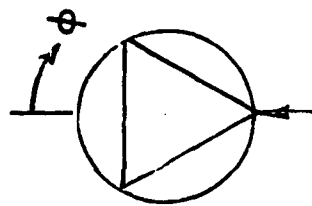
The inflection in the distribution near $x/L = .83$ reflects information obtained from schlieren photographs of the shock wave locations.

The pressures measured on the cylindrical surface between the flats are also shown in Figure 9 and very closely follow the centerline of the flat data. It is interesting that the cylindrical pressures decrease along with the centerline pressures as x/L approaches the afterbody junction even though there is no discontinuity in the surface for the cylindrical region. Between the flat surfaces the afterbody is a straight extension of the forebody cylinder. The effect of the nearby flat appears to cause lateral turning of the flow on the cylinder toward the flat with a consequent pressure drop on the cylinder. Unfortunately, pressure taps were not installed far enough forward to determine whether or not the minimum pressure coefficient on the cylinder corresponds to that on the flat.

It might be noted that attempts have been made to calculate supersonic flows on asymmetric configurations using axisymmetric formulations applied on longitudinal rays with the same local body geometry as the non-symmetric body. Such an assumption apparently will not work at transonic speeds because of the stronger effects of three-dimensionality.

A circumferential distribution of pressure coefficients is shown in Figure 10 for the most densely instrumented longitudinal station ($x/L = 0.881$). Note that symmetry has been used to define the curves more completely. Since taps were unsymmetrically arranged relative to the flat centerline, image data points were obtained by reflection through the centerlines and also data taken

MACH NO. = 0.94
 $\alpha = 0^\circ$
 $x/L = 0.881$



ϕ (DEGREES)

Figure 10. Circumferential pressure distribution at $M = 0.94$, $x/L = 0.881$ triangular afterbody model.

on one flat were assumed to represent the distribution on all three flat surfaces. A number of check pressures were obtained which indicated excellent agreement between corresponding points on the model. Flow angularity in the TPT tunnel was expected to be small.

The junction between the flat and the cylindrical surfaces are noted on the figure. The minimum pressure coefficient at this station was detected by the two taps nearest the junction and the curves were drawn assuming the minimum C_p is associated with the flow direction change at the corner.

Figure 11 shows a composite of all the zero angle of attack circumferential pressure coefficients for all the longitudinal stations. The size of the flat relative to the cylindrical surface increases as one moves back on the afterbody and at the same time the general pressure level increases consistent with the longitudinal centerline distribution already considered in Figure 9. Note that all the pressures on the flat surface are influenced by the corners at $x/L = 0.791$ where as at the downstream stations the effect of the corners appears to be limited to 10° to 15° circumferential angle.

Zero Angle of Attack - Mach Number Effects

Figure 12 shows the pressure coefficient distribution on the centerline of the flat surface for three Mach numbers, $M=0.90$, 0.94 and 0.97 . The cylindrical surface pressure clearly follows these data and therefore are not shown.

The curves drawn through the measurements are influenced by schlieren photographs of the flow fields shown in Figure 13, 14 and 15. Although knowledge of complicated three dimensional transonic flow fields such as these is limited, the figures suggest that a shock wave is generated downstream of the most forward junction of the afterbody and that the three dimensional expansion flow field results in a nearly normal shock surface at a fixed x/L station. The position of the shock wave moves back and increases in

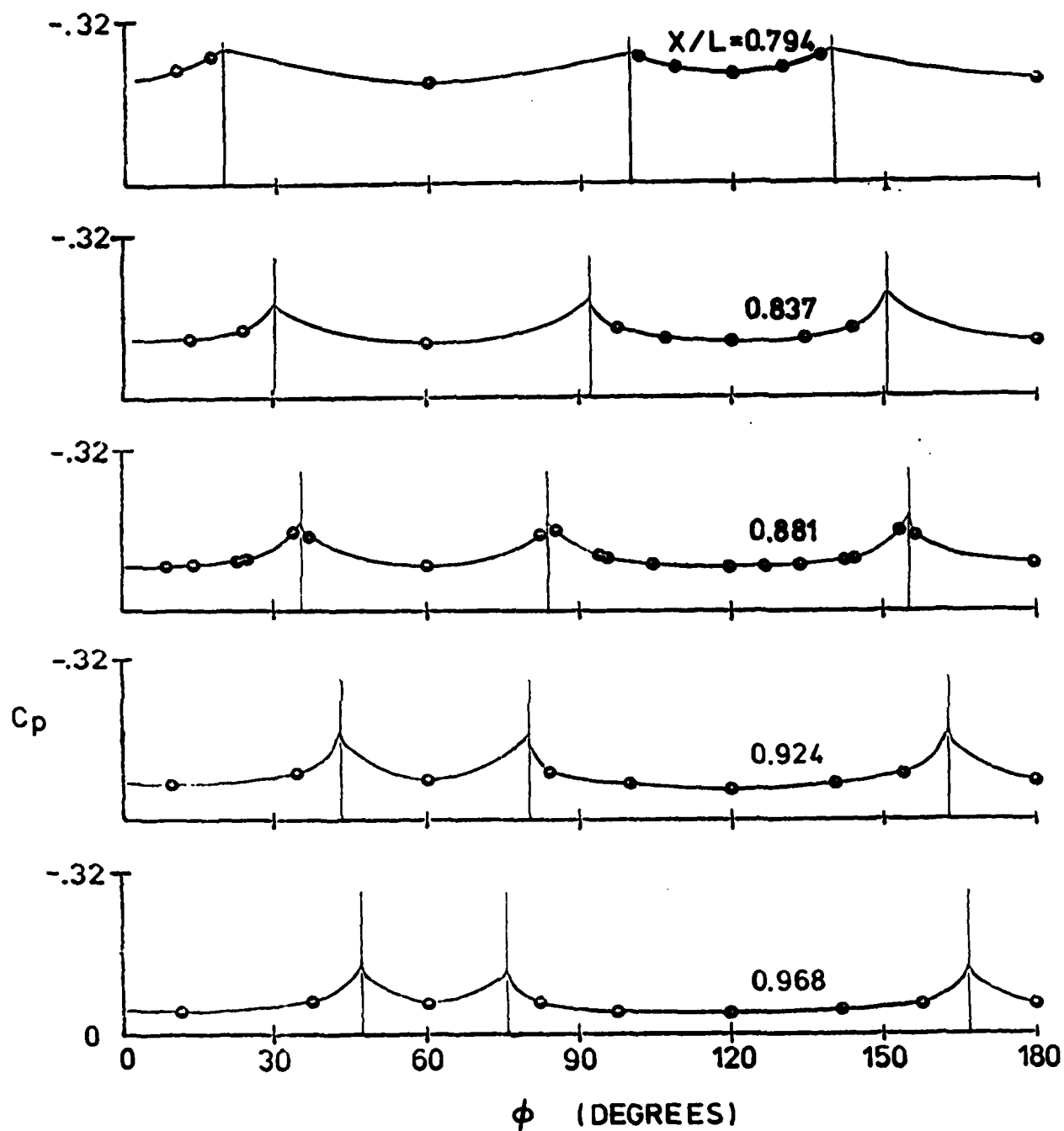


Figure 11. Circumferential pressure distribution at $M = 0.94$ all x/L stations, triangular afterbody model.

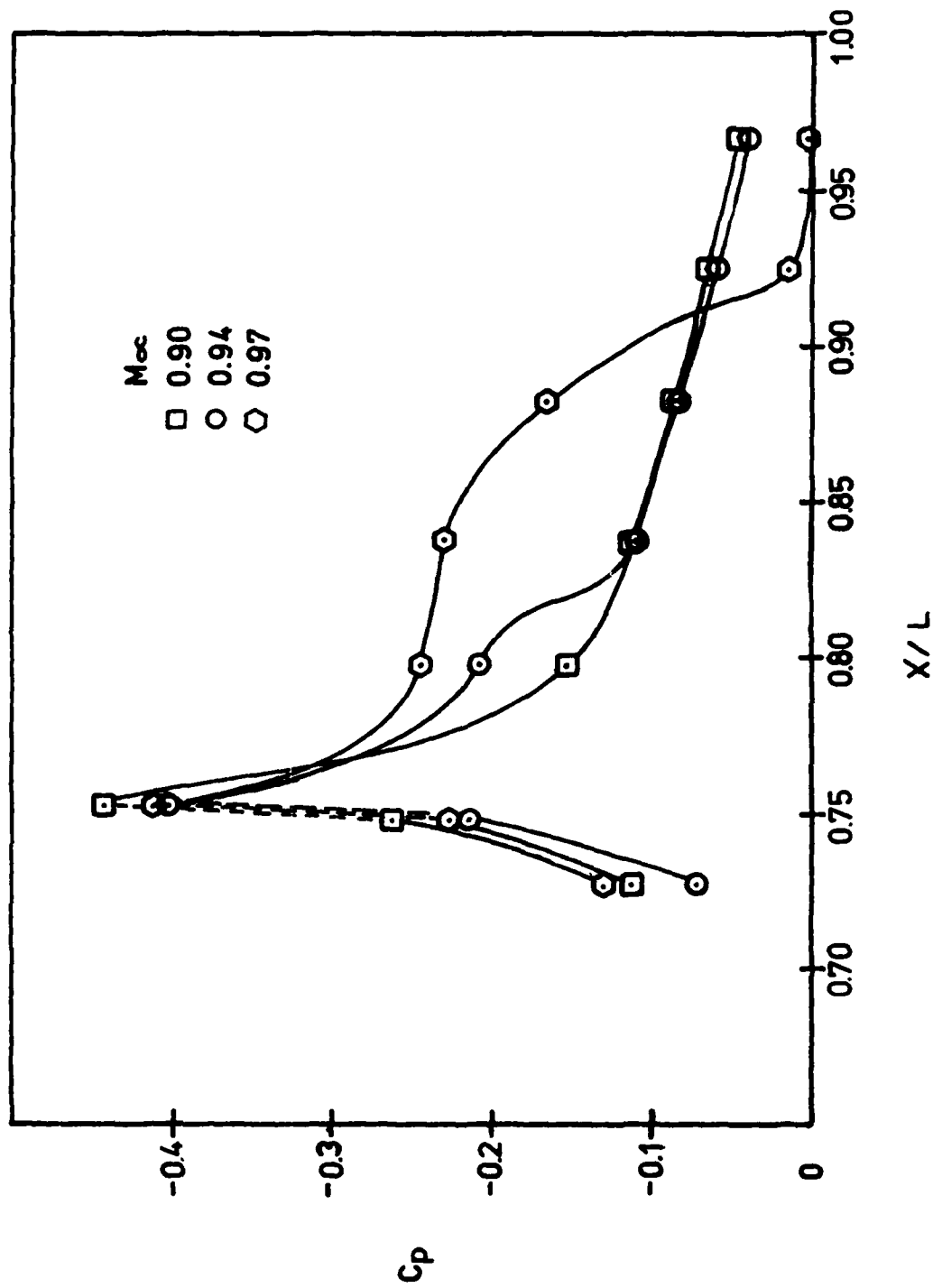


Figure 12. Effect of Mach number on the longitudinal pressure distribution.



Fig. 13 Schlieren photograph of afterbody flow field
 $\alpha=0^\circ$, $\phi=0^\circ$, $M=0.90$.



Fig. 14 Schlieren photograph of afterbody flow field
 $\alpha = 0^\circ$, $\phi = 0^\circ$, $M = 0.94$.

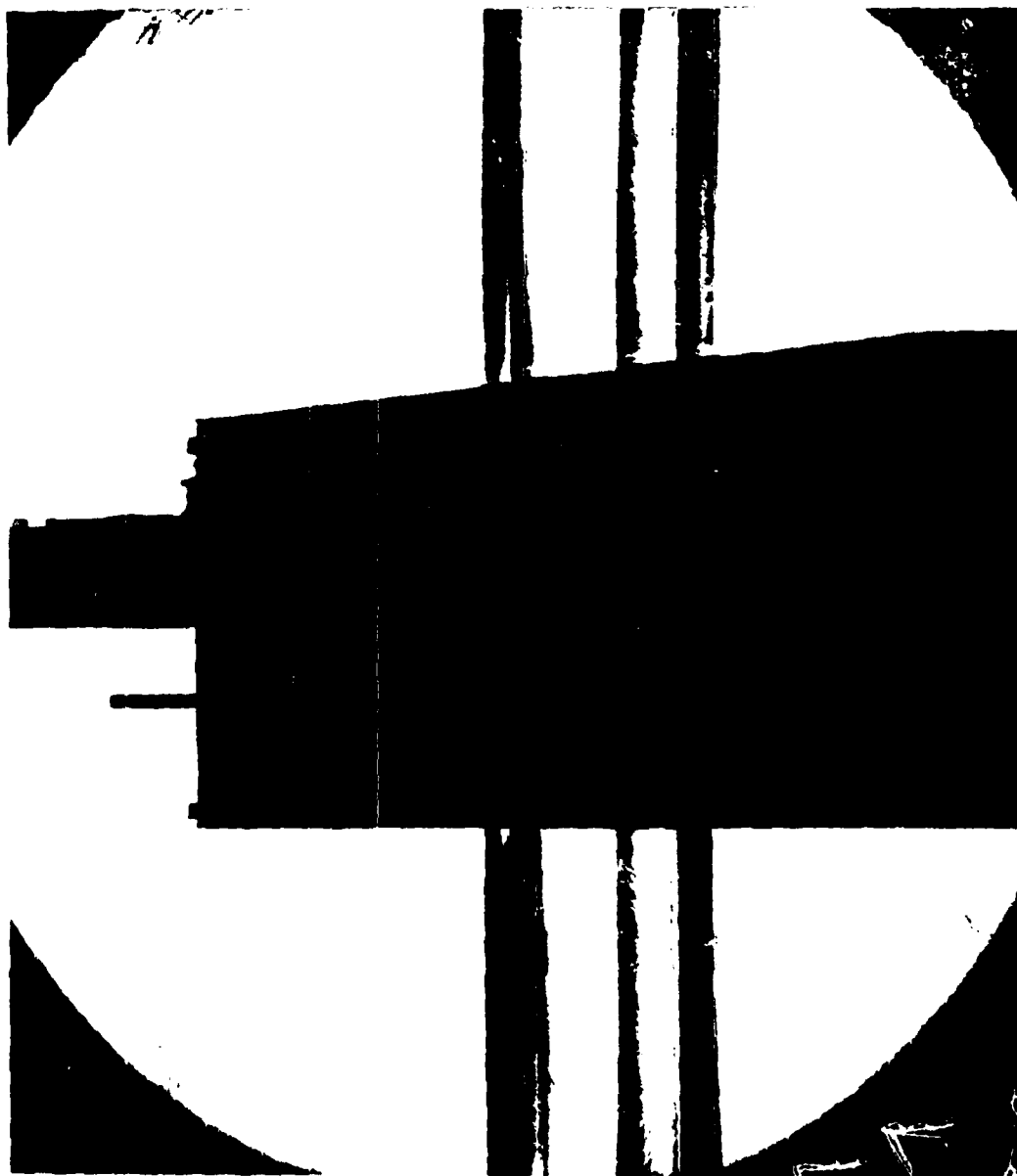


Fig. 15 Schlieren photograph of afterbody flow field $\alpha=0^\circ$, $\phi=0^\circ$, $M=0.97$.

strength with increasing free stream Mach numbers.

Comparison Between Triangular, Conical and Cylindrical Afterbody Pressure Distributions

The pressure distributions for the conical and cylindrical afterbodies are compared to that obtained for the triangular boat-tail in Figure 16. The forebody is the same for all three configurations as were the test conditions of $M=0.94$ and model total length. To achieve comparable base areas the triangular boattail must begin considerably further forward than the conical. In this case the conical model has a one half caliber boattail, whereas the triangular flats begin 1.446 calibers ahead of the base. The lowest pressure is slightly less for the triangular afterbody and it is more limited in extent, but more significant is the fact that the low pressure region and its terminating shock wave occur at x/L values of 0.75-0.80 for the triangular model as compared to 0.90-0.95 for the conical model. The closer the low pressure region is to the model center of gravity the less severe is the effect of pressure distribution on the projectile stability.

Zero Angle of Attack - Boundary Layer Profiles

As indicated previously a series of boundary layer profile measurements were made using a three probe rake and these measurements were repeated and extended using a more streamlined single probe. It was hoped that the rake would provide data on the circumferential boundary layer characteristics provided that interference effects between probes and its massive support would not be too severe. Initial tests showed that there was some effect on the model static pressure distribution and examination of the reduced velocity distributions show that close to the model surface there is up to 10% difference between the single probe and the rake data. Figure 17 shows a comparison between the centerline probe of the

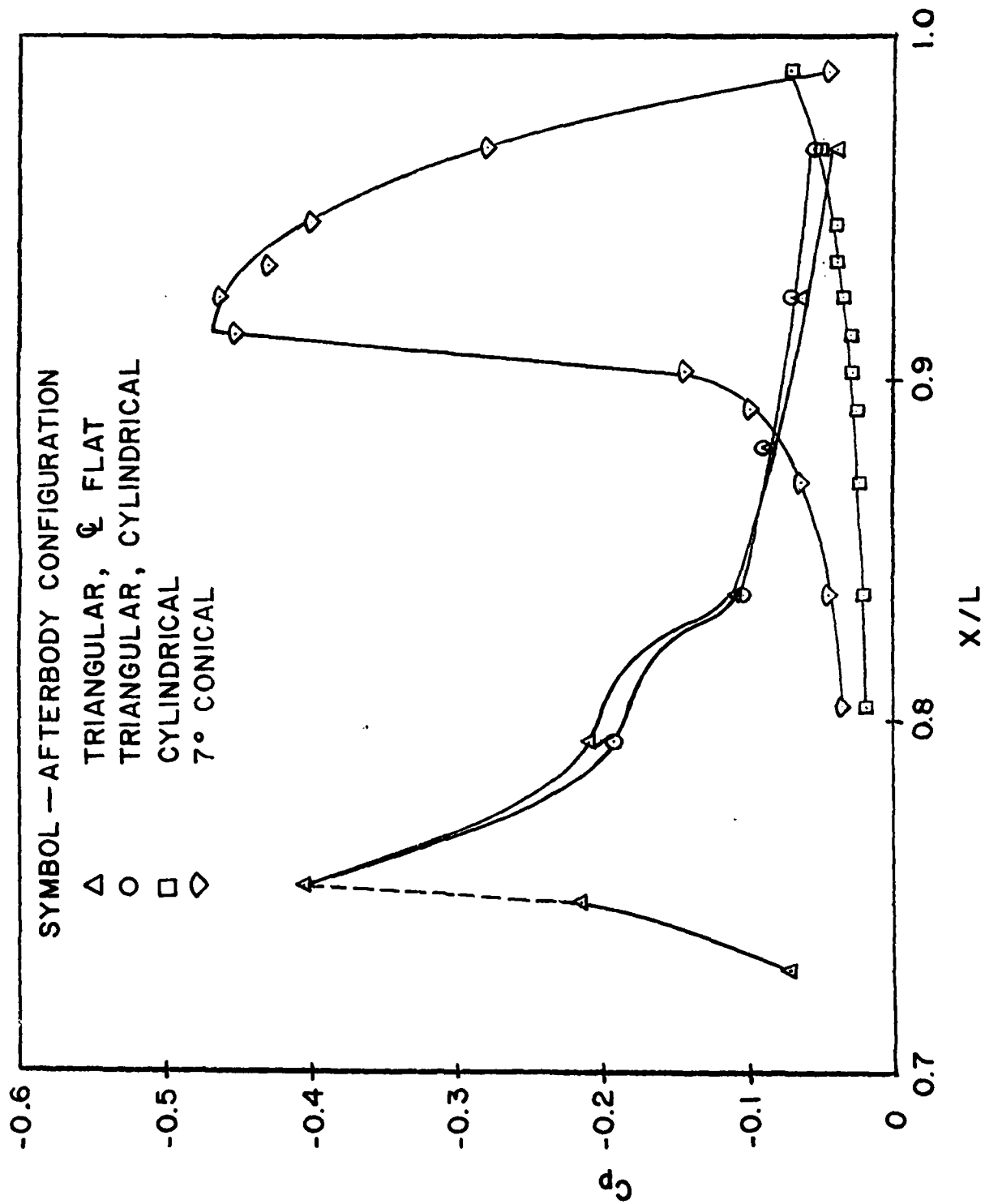


Figure 16. Comparison between pressure distribution measured on conical, cylindrical and triangular afterbodies.

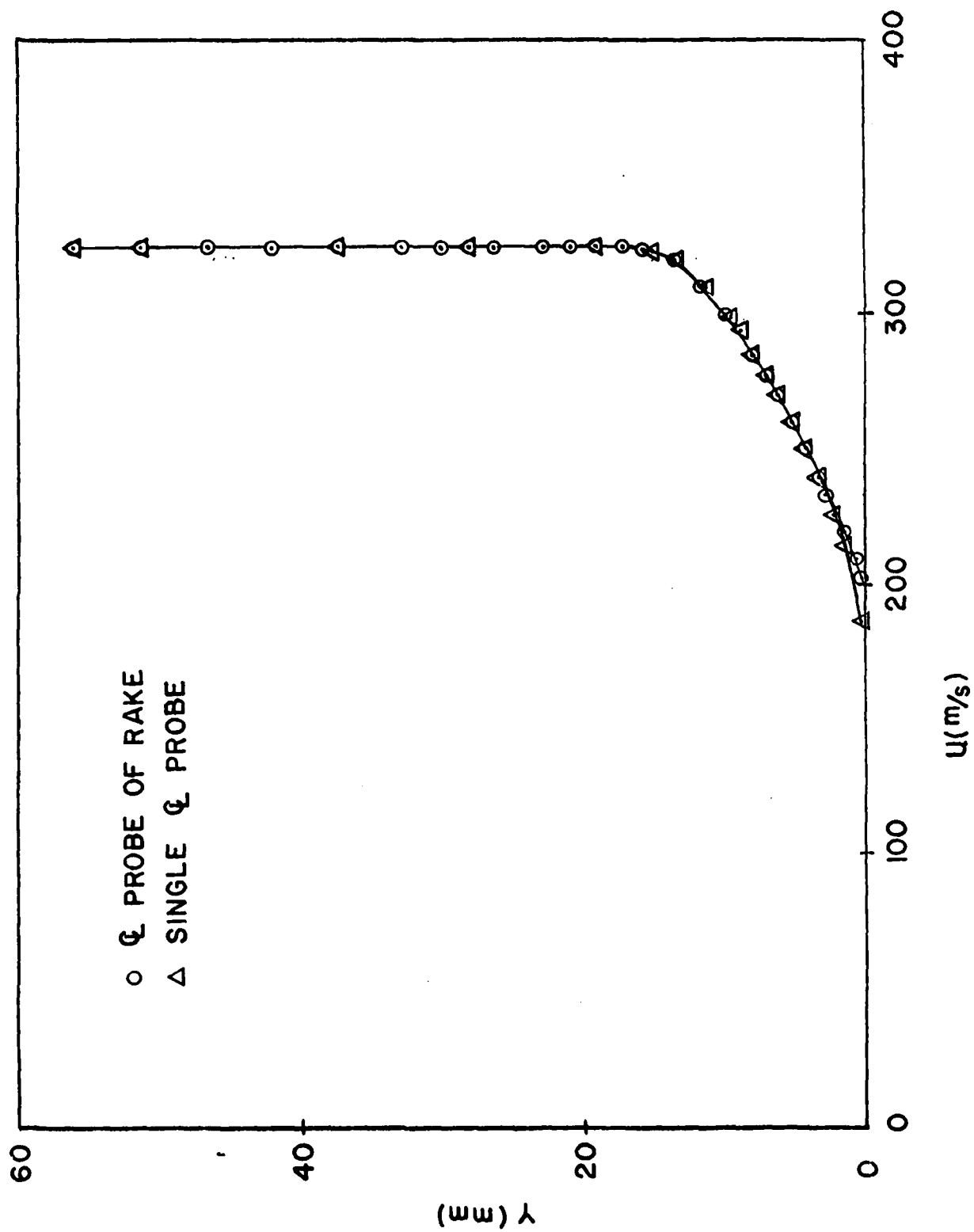


Figure 17. Comparison between rake probe and single probe boundary layer velocity profiles.

rake and the single probe velocity profile. Note that the agreement is excellent except within about 1mm of the wall. The effect of the rake on the wall static pressure indicates an upstream static pressure rise of 10% at 5cm ahead of the probe and this decreased to less than 1% at the most forward position on the flat. Similar upstream effects were observed with the single probe but reduced in magnitude by a factor of one half. It is assumed that the viscous flow encountered by the probe is effected by this amount of interference and that the velocity profiles should be interpreted with this in mind.

The total head pressure measurements were reduced to velocity assuming constant static pressure through the boundary layer as measured on the model without the probe installed. The isentropic impact pressure formula was used to calculate a local Mach number. The total temperature was assumed constant across the boundary layer in determining the local velocity of sound. No connection for local flow angularity was attempted. In some situations, particularly at angle of attack and some roll positions, this could influence the results. Attempts to measure the flow angle were unsuccessful. Since the pitot probes are insensitive to small angles, the results are interpreted as longitudinal velocities.

Figure 18 shows the three velocity profiles measured with the rake at station $x/L = 0.881$. Probe 2 is the centerline probe and probes 1 and 3 were located unsymmetrically with respect to the middle probe. Note that probe 3 was the farthest from the centerline and is in the thinnest boundary layer as might be anticipated from the pressure distribution data.

A boundary layer survey was also made at a second longitudinal station ($x/L = 0.924$) using only a single probe. The velocity profile at that station is shown in Figure 19 along with the centerline profile from station $x/L = 0.881$. The thickening of the boundary layer is apparent.

Table 3 summarizes boundary layer thicknesses and shape factors calculated from the triangular afterbody velocity profile measurements. Figure 20 shows the distribution of total boundary layer

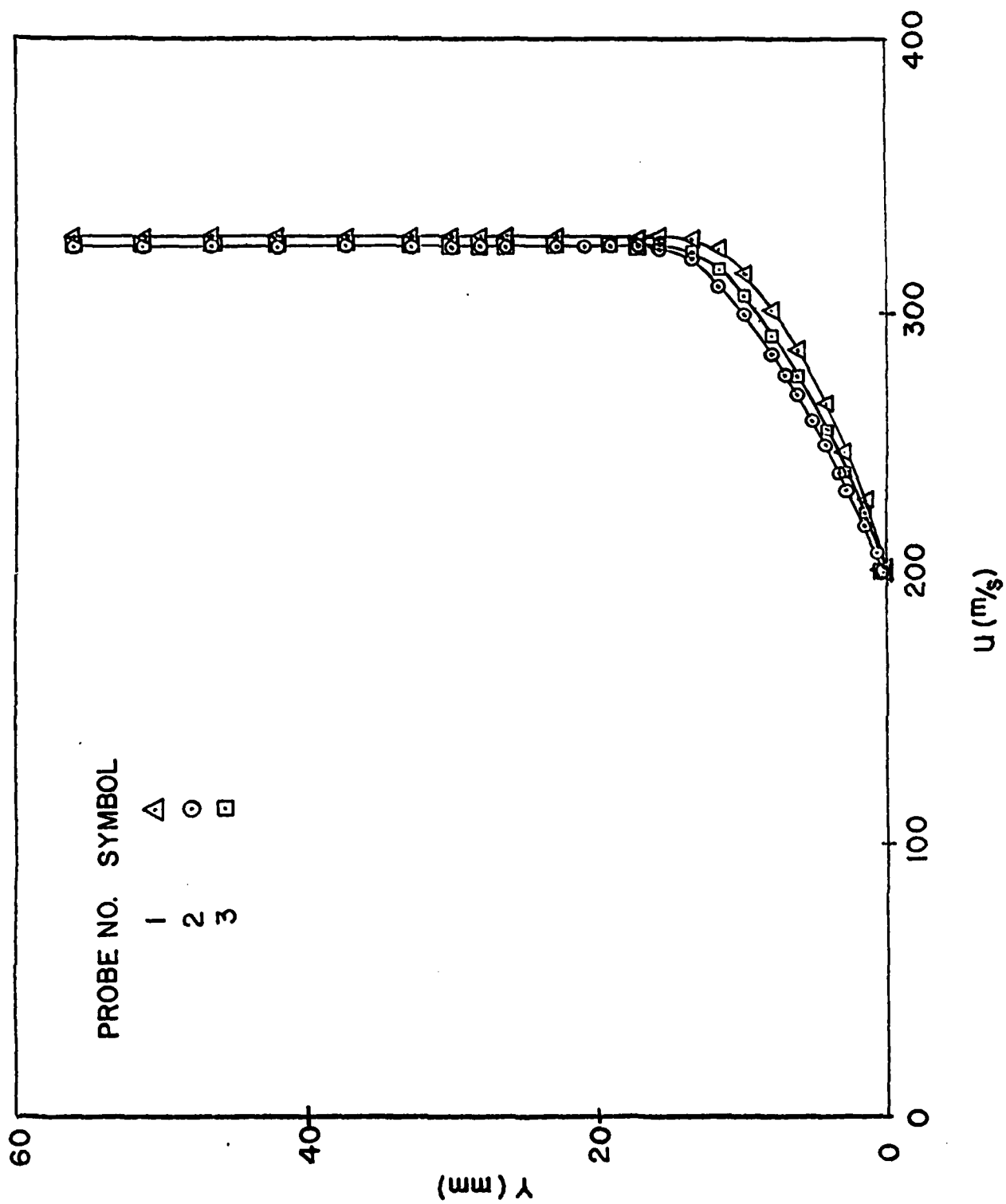


Figure 18. Velocity profiles at $x/L = 0.881$, $\alpha = 0^\circ$, $M = 0.94$.

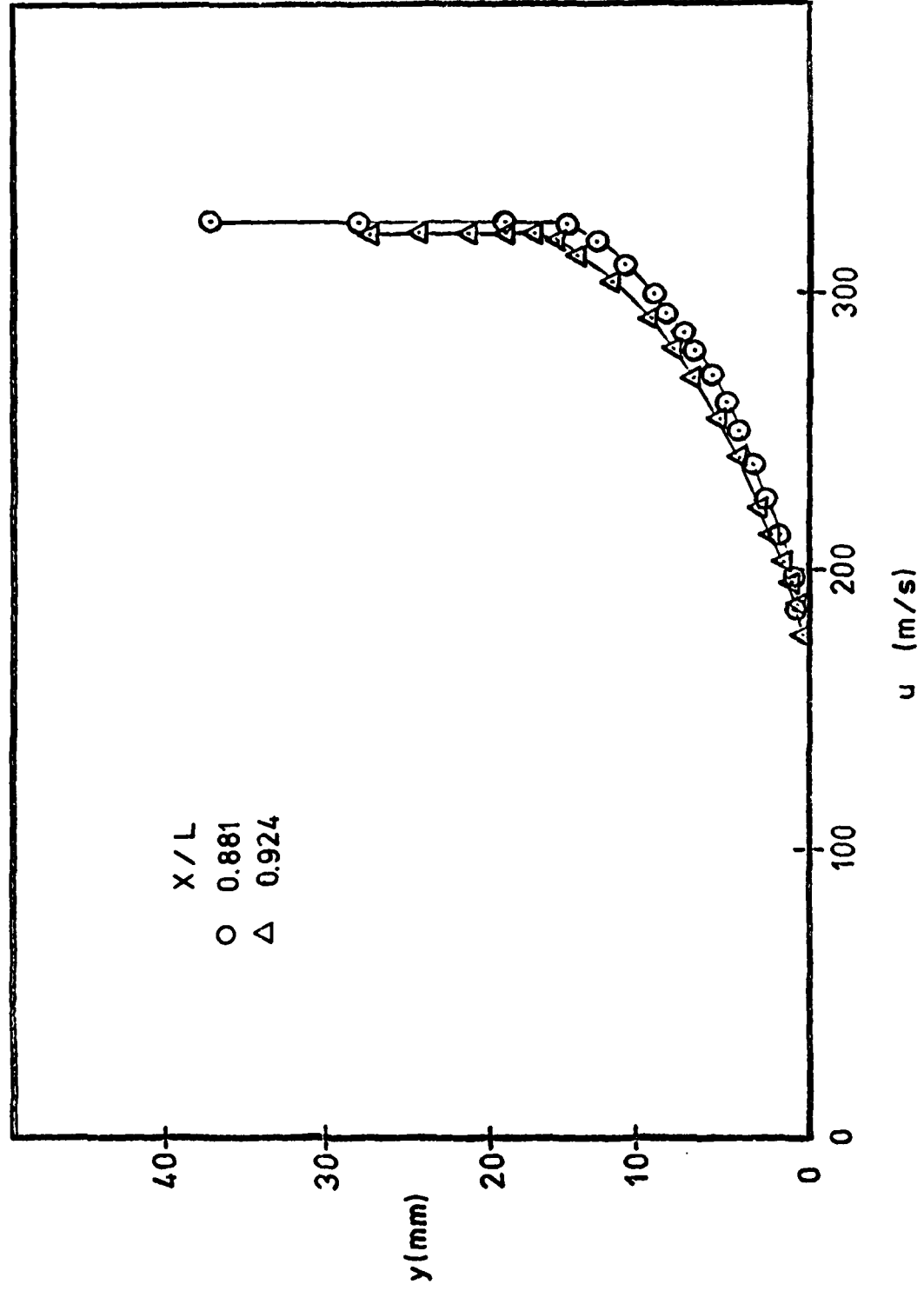


Figure 19. Centerline velocity profiles at two longitudinal stations, $x/L = 0.881$ and 0.924 , $\alpha = 0^\circ$, $M = 0.94$.

TABLE 3. BOUNDARY LAYER PROPERTIES TRIANGULAR AFTERBODY

Zero Angle of Attack

 $M = 0.94, \alpha = 0^\circ$

x/L		0.881			0.924	
ϕ	0	14.3	24.8	0	60	0
Probe	2 ⁽¹⁾	3	1	ξ ⁽²⁾	CYL	ξ
δ	14.3	13.5	12.2	14.2	8.7	15.6
δ_x^*	2.8	2.5	2.2	2.8	1.3	9.1
θ_x	1.6	1.5	1.3	1.6	0.8	1.7
H_x	1.75	1.73	1.73	1.76	1.67	1.77

(1) Centerline probe in 3-probe rake.

(2) Duplicates ξ measurement using a single probe.

thickness at the $x/L = 0.881$ station. Because of the limited number of profiles obtained, the behavior near the flat-cylinder function should be considered tentative.

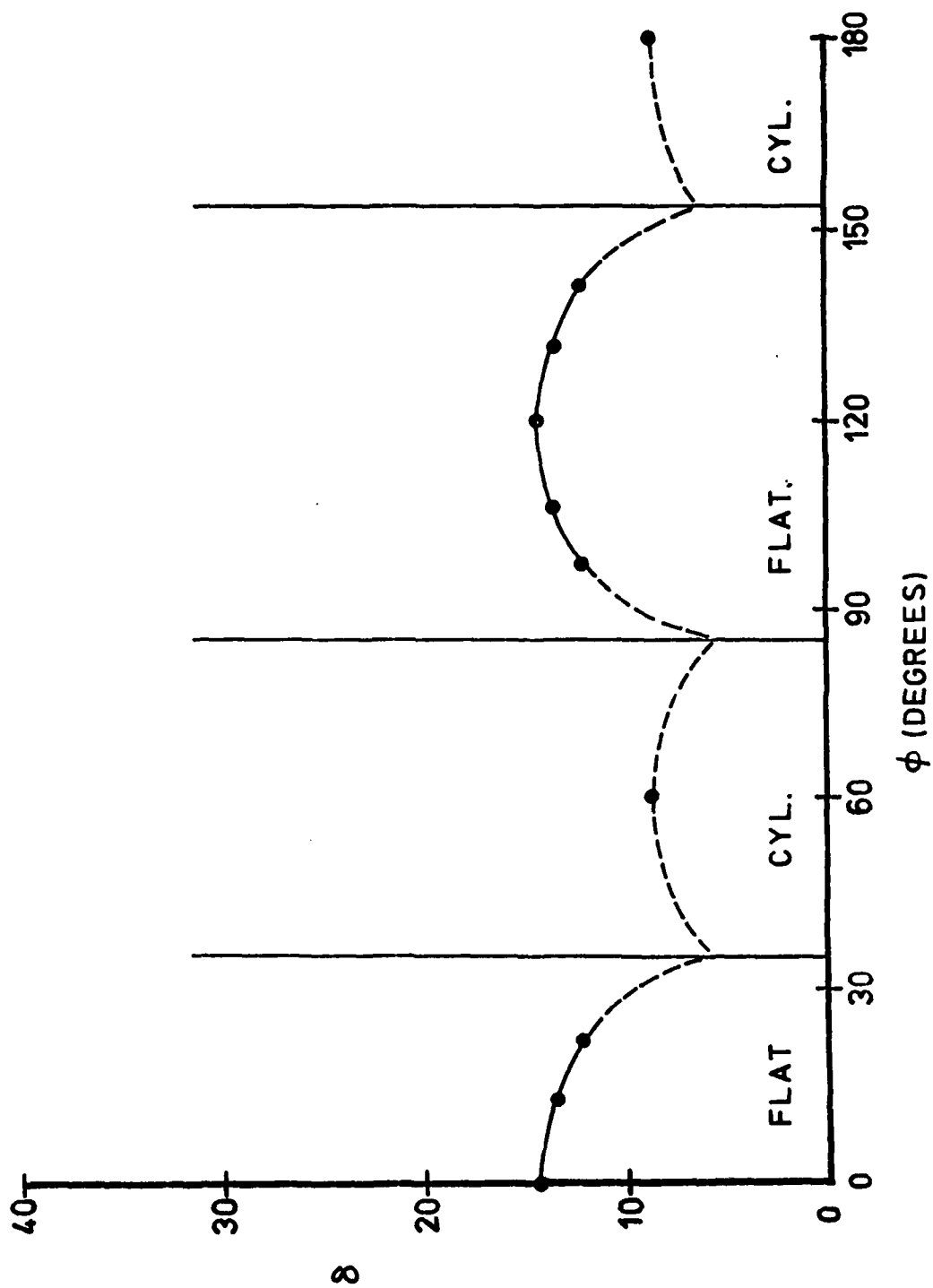


Figure 20. Total boundary layer thickness as a function of circumferential position at $x/L = 0.881$, $\alpha = 0^\circ$, $M = 0.94$.

RESULTS - ANGLE OF ATTACK

In this section the measured effects of angle of attack on the aerodynamic characteristics of the triangular afterbody are presented. Of primary interest are the pressure distribution and boundary layer characteristics. Because of the time consuming nature of the boundary layer measurements only 4° angle of attack has been investigated. This angle was selected as representative of the situation where the flow is everywhere attached to the model and not so large as to produce major vortical flows.

Circumferential Pressure Distribution

As pointed out in the description of the model and experiment, three orientations of the asymmetric model were considered at angle of attack as shown in Figure 5. These orientations are specified for the experiments in terms of the location of the instrumented flat with respect to the lee side of the model. Although measurements were made at $\alpha = \pm 4^\circ$ and at $\phi = 0^\circ, \pm 30^\circ$ and $\pm 60^\circ$ of roll, all the data can be associated with $\alpha = +4^\circ$ and either $0^\circ, +30^\circ$ and $+60^\circ$ of roll. Zero roll, configuration A, has a flat on the lee side and a point of the triangle on the windward side. $\phi = 60^\circ$, configuration B is the reverse with a flat to windward. Both configuration A and B result in a symmetric cross sectional shape with respect to the cross flow. Configuration C is different in that the flat is parallel to the model pitch plane.

Figures 21 and 22 show the circumferential pressure distributions at the five longitudinal stations. A mach number of 0.94 applies to all these data. The shape of the curves drawn through the measured data points is guided by the results at the $x/L = 0.881$ station where the largest number of pressure taps were located circumferentially. Figure 21 shows the data for configuration A. In that configuration the minimum pressure coefficient is observed to occur at the junction between the windward inclined

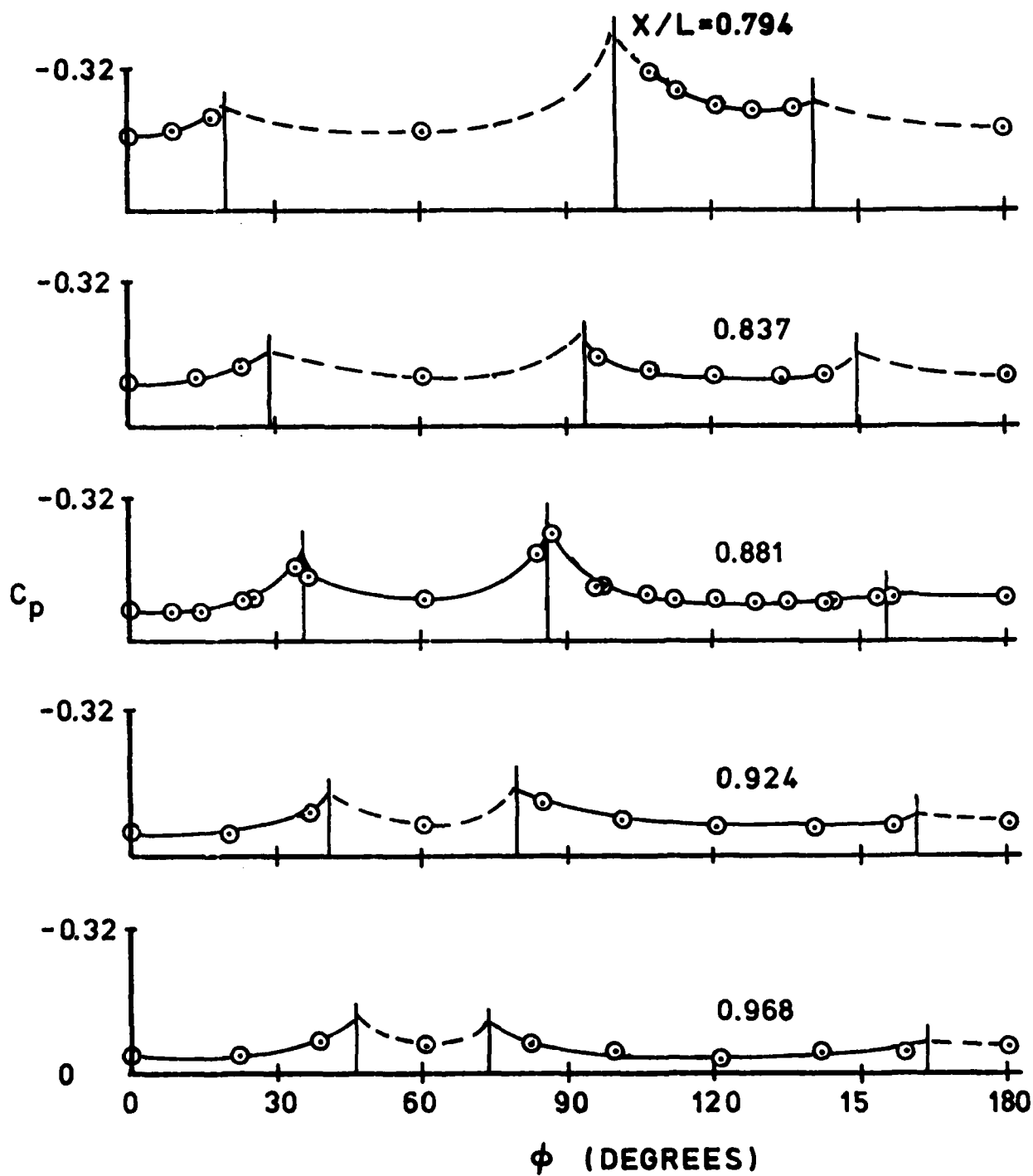


Figure 21. Circumferential distribution of pressure coefficients on triangular afterbody in Orientation A for five longitudinal stations ($M_\infty = 0.94$, $\alpha = 4^\circ$).

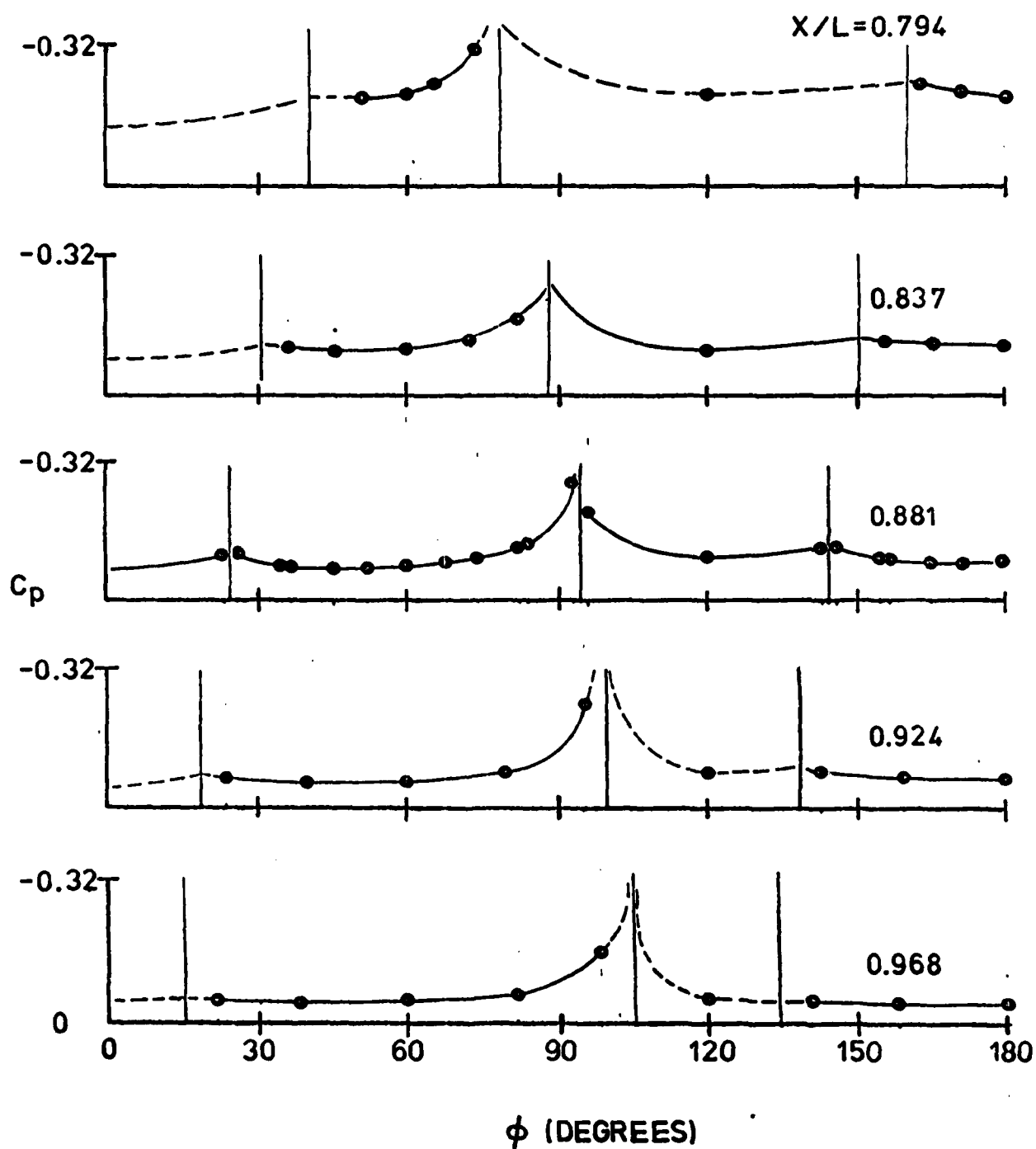


Figure 22. Circumferential distribution of pressure coefficients on triangular afterbody in Orientation B for five longitudinal stations ($M_\infty = 0.94$, $\alpha = 4^\circ$).

flat and the cylindrical section ($\sim 90^\circ$) next to the lee side. In contrast to the symmetric variation of pressure on the flat and cylindrical section in the $\alpha = 0$ case, the pressure on the windward flats ($\phi = 120^\circ$) are quite unsymmetric and show practically no change in pressure at the windward side cylindrical junction.

Figure 22 shows the data for configuration B with a flat to windward. The lowest pressure region is basically in the same angular position relative to the lee side, or 80 to 110° from the lee side.

Boundary Layer Characteristics

Table 4 and Figures 23 and 24 present the boundary characteristics obtained from the rake and single probe surveys. The figures show the total boundary layer thickness determined at the point where the local velocity equals 99% of the boundary layer edge velocity. The velocity at the outer edge was easily determined because of the nearly constant total head pressure. Figures 17-19 show typical profiles and additional examples from the angle of attack experiments differ only in scale and minor details. The scale of the boundary layer is shown in Figure 23 for the configuration A and in Figure 24 for configuration B. All these measurements are for $M = 0.94$, $\alpha = 4^\circ$ and $x/L = 0.881$. The circumferential position is measured from the model lee side. Because of the time consuming nature of the probing technique, only representative surveys could be obtained and the dashed lines drawn through the data points indicate tentative distributions. These are particularly uncertain in the vicinity of the flat-cylinder junctions where the acceleration of the flow is expected to produce the thinnest profiles. The lee side profile for configuration A shows the thickest viscous layer by a factor of two of all the points investigated. The boundary layer at this point added to the model surface exceeds the radius of the circumscribing cylinder by 17%. The displacement thickness, however, is considerably smaller.

TABLE 4
BOUNDARY LAYER PROPERTIES
TRIANGULAR AFTERBODY

CONFIGURATION A
 $M = 0.94$, $\alpha = 4^\circ$

x/L	0.881						0.924	
ϕ	0	14.3	24.8	0	120	180	0	120
Probe	2 ⁽¹⁾	3	1	ζ ⁽²⁾	ζ	CYL	ζ	ζ
δ	35.3	22.8	17.6	38.0	10.2	5.4	35.5	10.6
δ^*	3.6	4.5	4.0	4.6	1.8	.7	4.8	1.8
θ_x	2.1	2.5	2.2	2.7	1.0	.4	2.8	1.1
H_x	1.67	1.78	1.82	1.69	1.72	1.63	1.69	1.71

(1) center line probe in 3-probe rake.

(2) duplicates ζ measurement using a single probe.

CONFIGURATION B
 $M = 0.94$, $\alpha = 4^\circ$

x/L	0.881									
ϕ	35.2	45.7	60.0	74.3	84.8	120.	155.2	165.7	180	180
Probe	1	3	2 ⁽¹⁾	3	1	CYL	1	3	2 ⁽¹⁾	ζ ⁽²⁾
δ	11.0	13.4	14.4	15.2	14.0	6.0	7.9	9.0	9.3	9.4
δ^*	2.2	2.5	2.9	3.1	2.7	.8	1.3	1.4	1.5	1.6
θ_x	1.2	1.4	1.6	1.8	1.6	.5	.8	.8	.9	.9
H_x	1.79	1.75	1.76	1.78	1.74	1.64	1.67	1.68	1.68	1.71

TABLE 4 CONT.

CONFIGURATION B
 $M = 0.94$, $\alpha = 4^\circ$

x/L	0.924	
δ	60	180
Probe	ζ	ζ
δ	15.8	10.2
δ^*		
δ_x	3.4	1.8
θ_x	1.9	1.1
H_x	1.81	1.72

CONFIGURATION C
 $M = 0.94$, $\alpha = 4^\circ$

x/L	0.881							0.924
δ	5.2	15.7	30	44.3	54.8	30	150	30
Probe	1	3	2 ⁽¹⁾	3	1	L ⁽²⁾	L	L
δ	13.6	17.7	18.5	20.4	22.3	18.3	9.5	20.4
δ^*								
δ_x	3.1	3.6	4.1	4.2	3.3	4.0	1.6	4.5
θ_x	1.7	2.0	2.3	2.4	1.9	.2	0.9	2.5
H_x	1.82	1.78	1.76	1.80	1.70	1.83	1.72	1.83

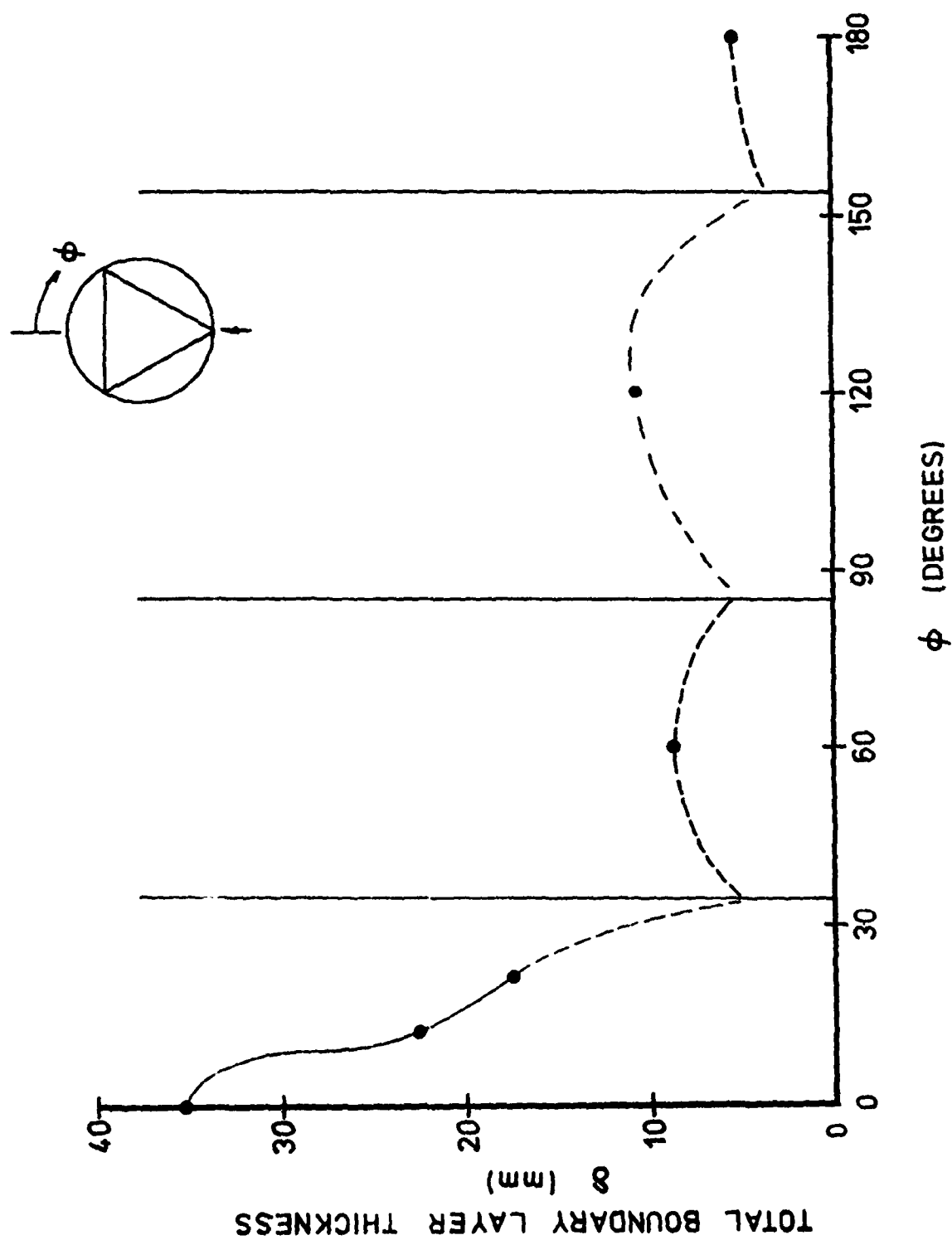


Figure 23. Circumferential distribution of boundary layer thickness on triangular afterbody in Orientation A ($M_\infty = 0.94$, $\alpha = 4^\circ$, $x/L = 0.881$).

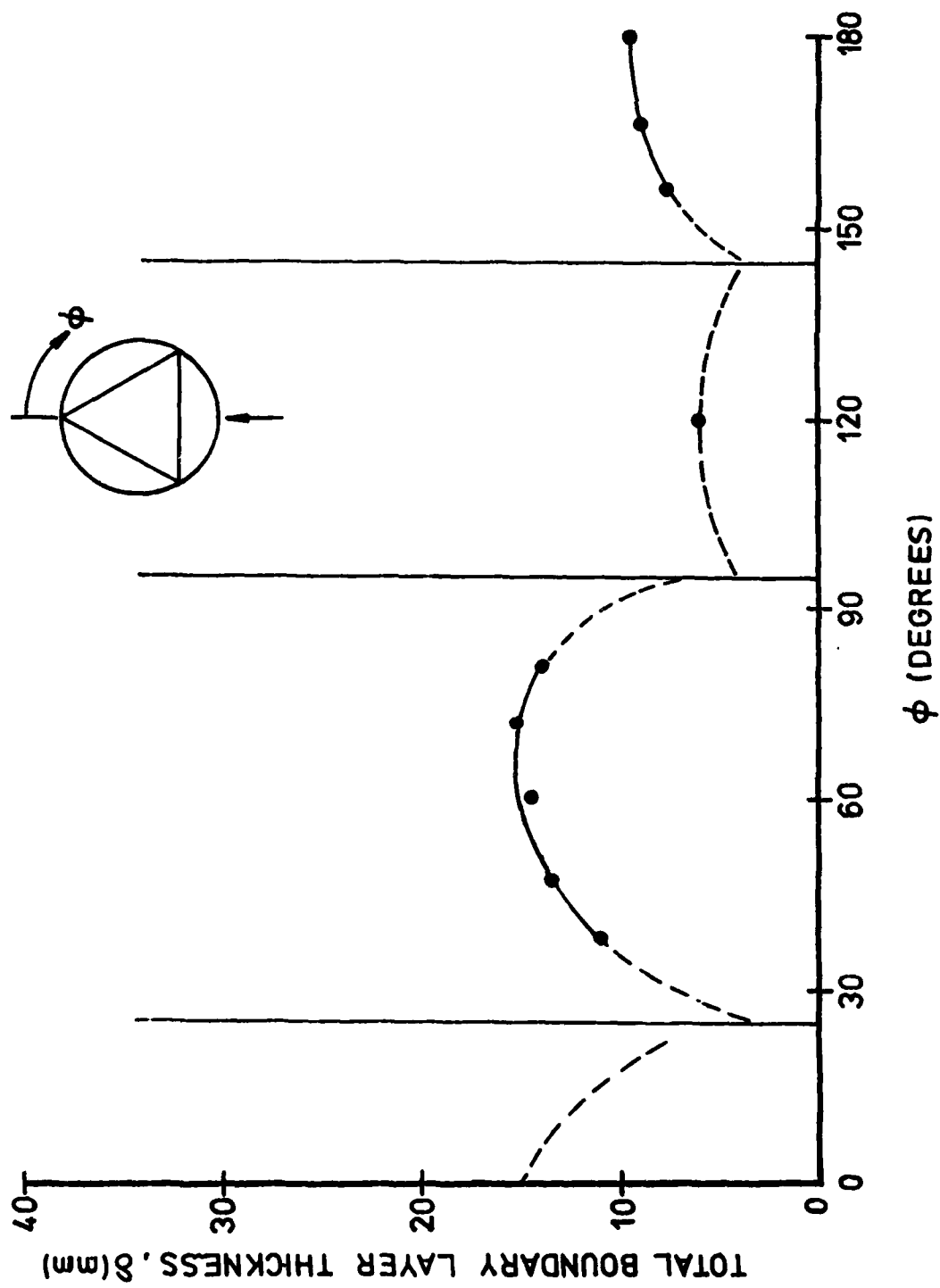


Figure 24. Circumferential distribution of boundary layer thickness on triangular afterbody in Orientation B ($M_\infty = 0.94$, $\alpha = 4^\circ$, $x/L = 0.881$).

The degree of asymmetry in the pressure distribution is illustrated by the side of flat data of configuration B where the asymmetric geometry of the probe rake was employed to provide the maximum detail.

Table 4 summarizes the boundary layer parameters obtained from the probe surveys. The longitudinal component of velocity has been used to calculate the equivalent two-dimensional displacement and momentum thickness which are defined as:

$$\delta_x^* = \int_0^{\delta} \left(1 - \frac{\rho}{\rho_e} \frac{U}{U_e}\right) dy,$$

$$\theta_x = \int_0^{\delta} \frac{\rho}{\rho_e} \frac{U}{U_e} \left(1 - \frac{U}{U_e}\right) dy$$

respectively. The quantity $H_x = \delta_x^* / \theta_x$ has also been calculated as a measure of profile shape.

DISCUSSION

Two factors are of main interest in considering non-axisymmetric projectiles; drag and pitching moment. As pointed out by Platou these are of particular significance at transonic speeds because of the major variation in these properties as the result of the appearance and movement of transonic shock waves. Figure 25 and 26 are reproduced from reference (1) of Platou to illustrate the general behavior of drag and pitching moments obtained from wind tunnel and ballistic range tests.

Conical Boattail Tests

Because of the limitations of the model used in the present tests attention is focused on the effect of the afterbody geometry on the aerodynamic properties. At transonic speeds there are usually two shock wave systems on ogive-cylinder-boattail configurations - one associated with the afterbody and an upstream shock near the ogive-cylinder junction. This upstream shock system is presumed to be only weakly, if at all, effected by the afterbody and thus its effect is assumed common to all configurations. Furthermore, the shock occurs near the normal center of gravity location and therefore contributes rather weakly to the moment and nothing at all to the drag.

In order to make comparisons between the triangular afterbody and other more conventional geometries, tests were made using the same model equipped with a cylindrical and 1/2 caliber, 7° conical afterbody. The results of these tests have been reported elsewhere.¹³ A sketch of the model with conical boattail is given in Figure 27 on which the pressure port locations are indicated.

Figures 28-31 summarizes the pressure distribution results obtained from these experiments. The first figure illustrates the Mach number tested and at $\alpha = 4^\circ$ the longitudinal distribution of pressure coefficient at three angular positions on the model. Lon-

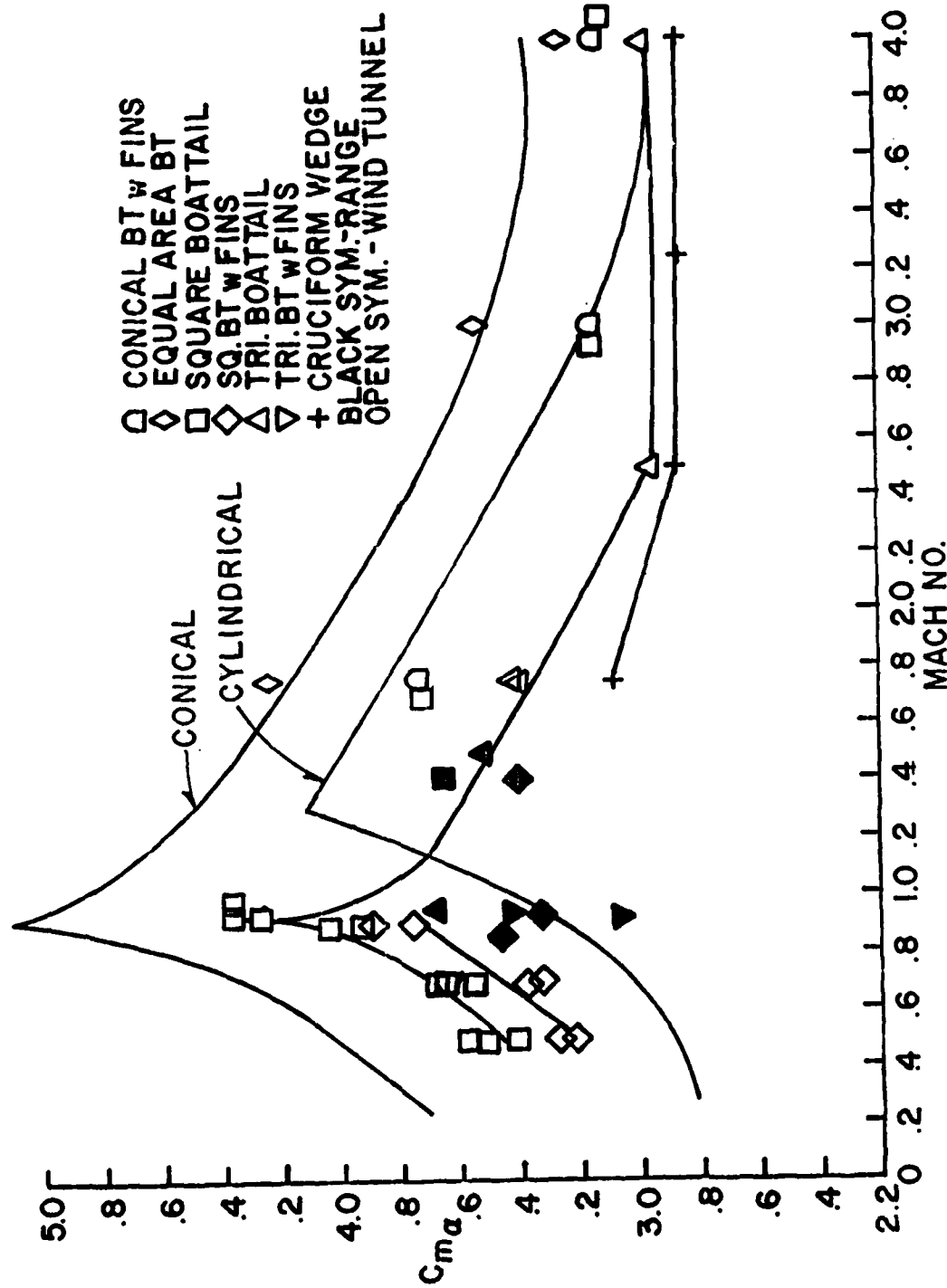


Figure 25. Pitching moment coefficient slope vs. Mach number for several afterbody configurations (Ref. 12).

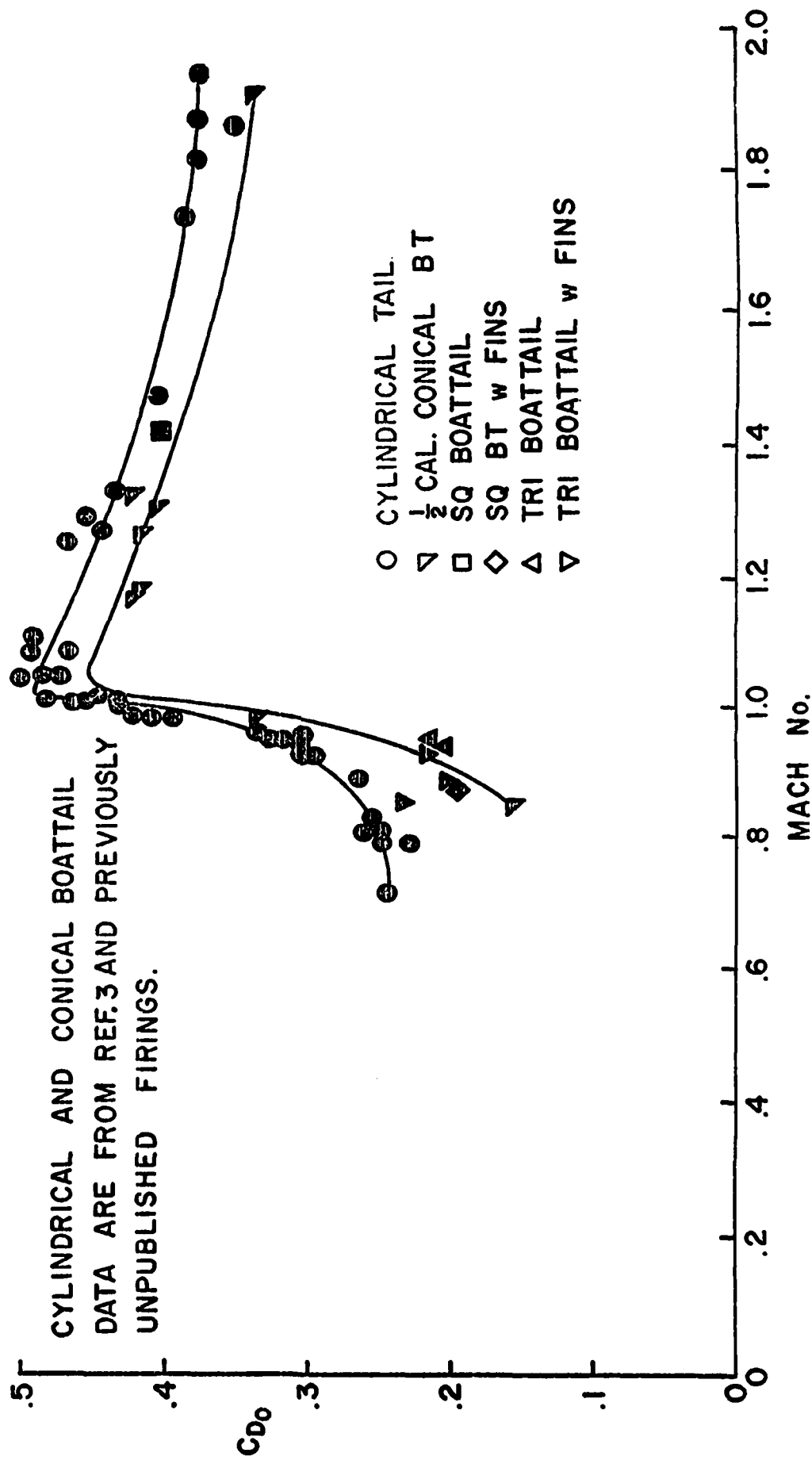


Figure 26.

Zero angle of attack drag coefficient for several afterbody configurations (Ref. 12).

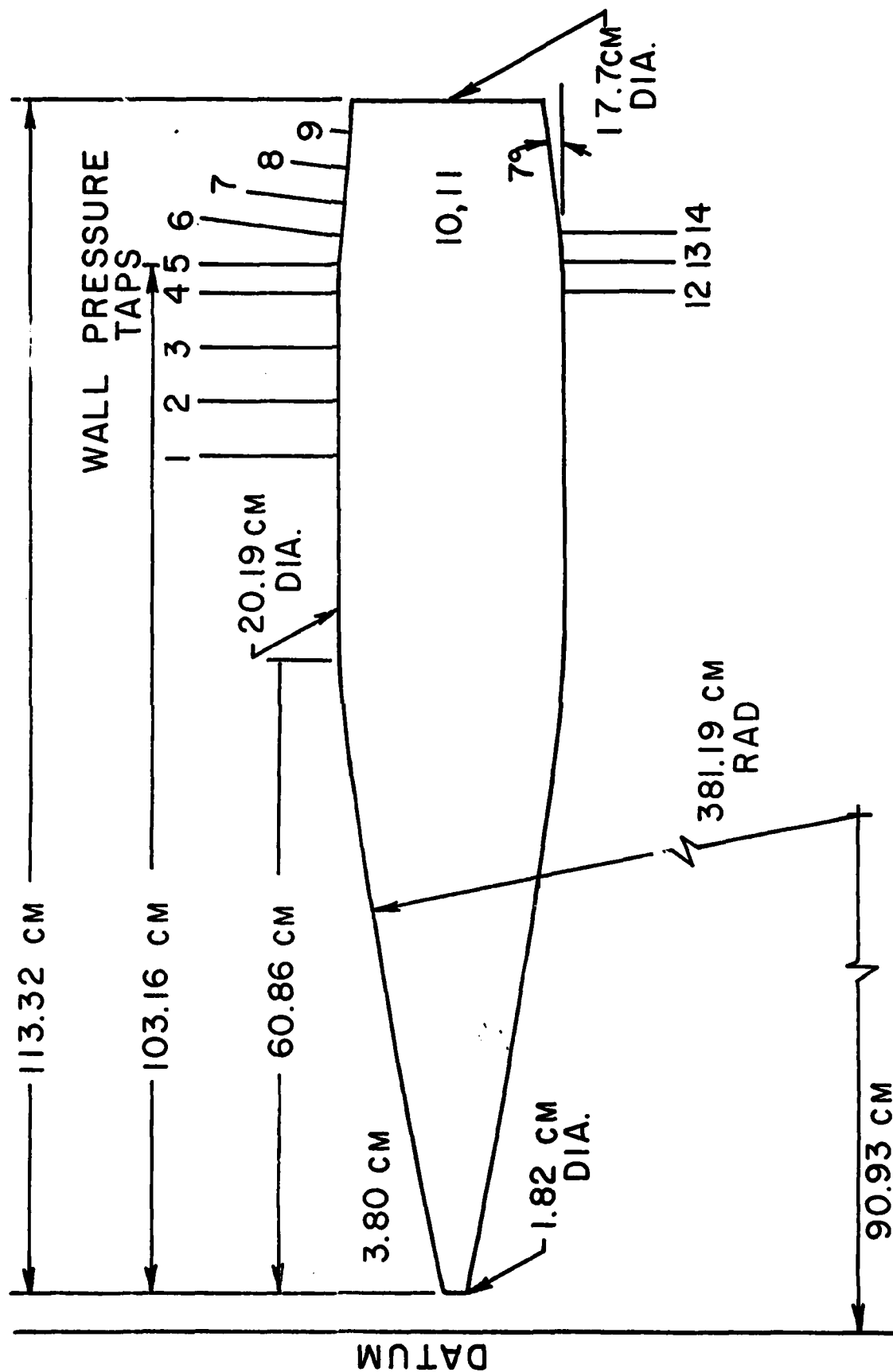


Figure 27. Conical boattail model configuration showing dimensions.

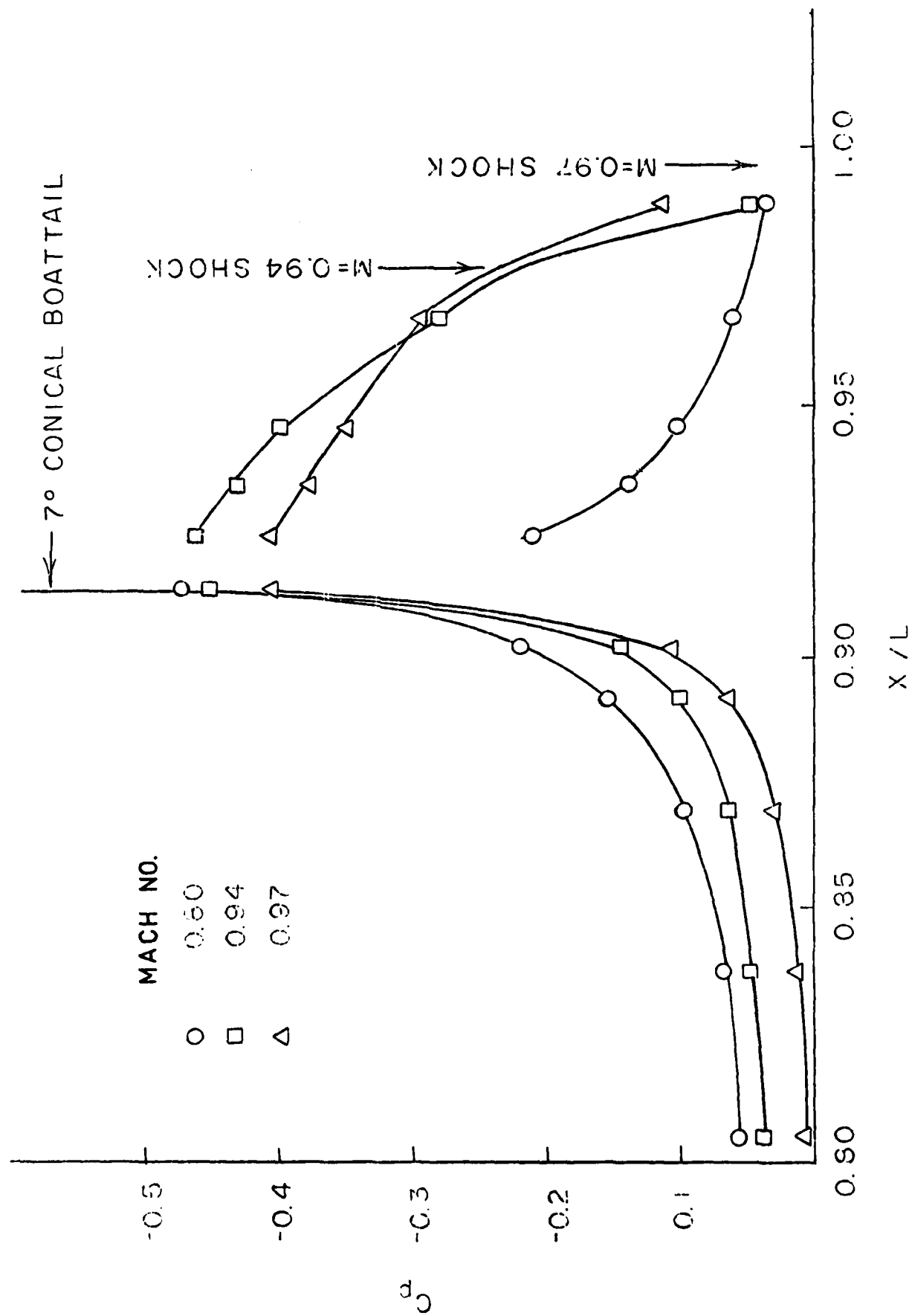


Fig. 20 Effect of Mach number on zero angle of attack pressure distribution for the conical boattail model.

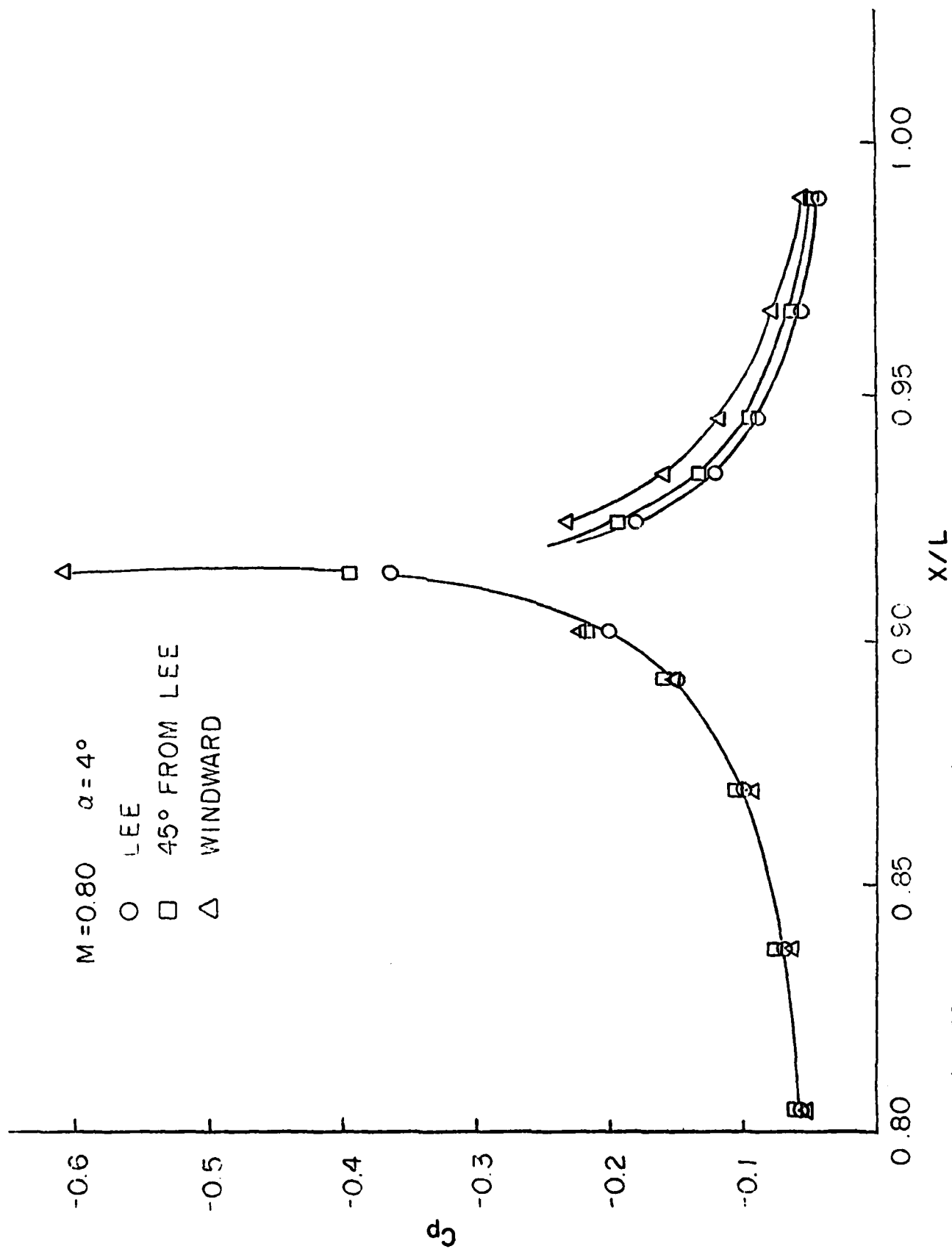


Fig. 29 Pressure coefficient distribution on conical boattail, $\alpha = 4^\circ$, $M_\infty = 0.08$.

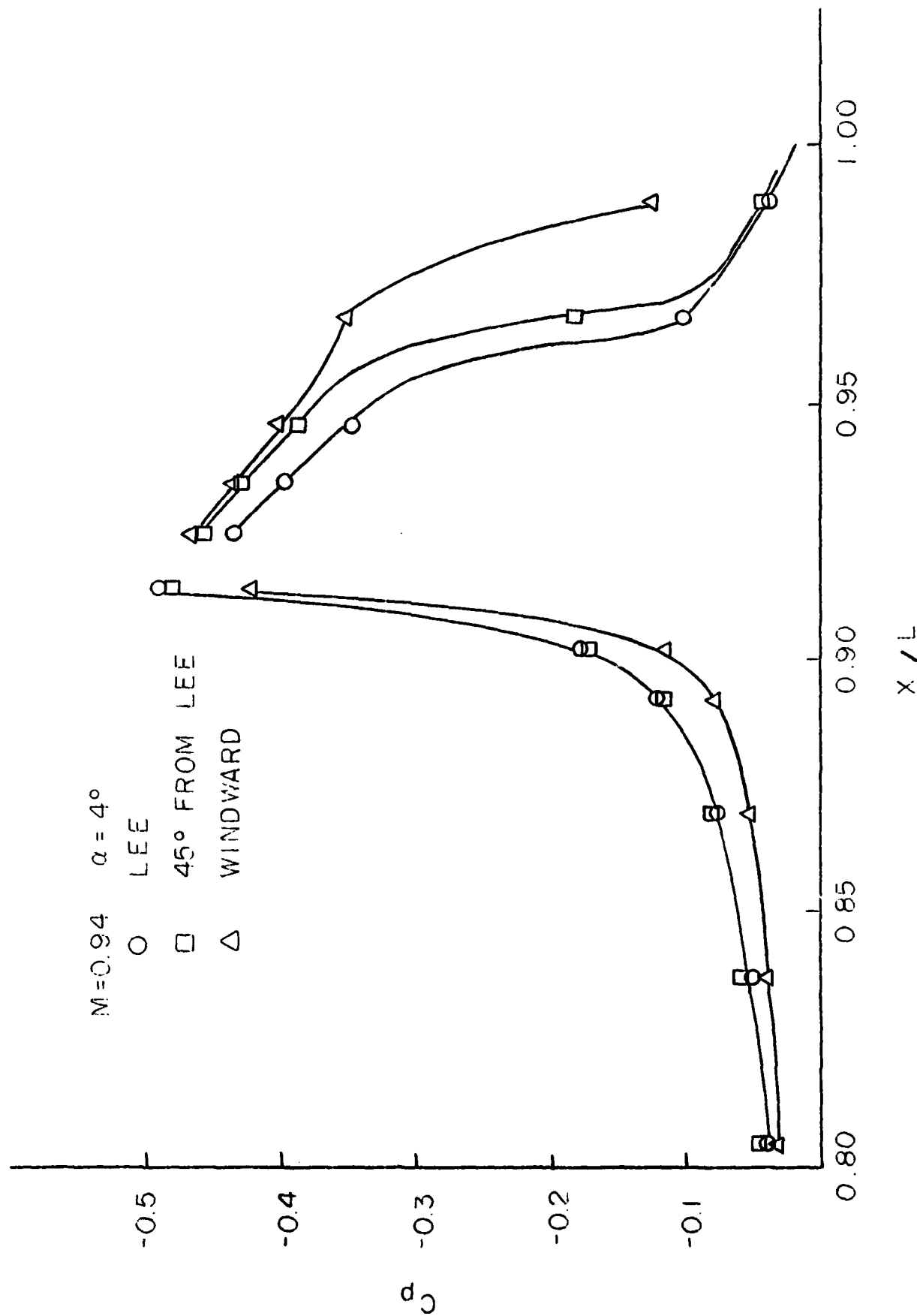


Fig. 30 Pressure coefficient distribution on conical boattail, $\alpha = 4^\circ$, $M_\infty = 0.94$.

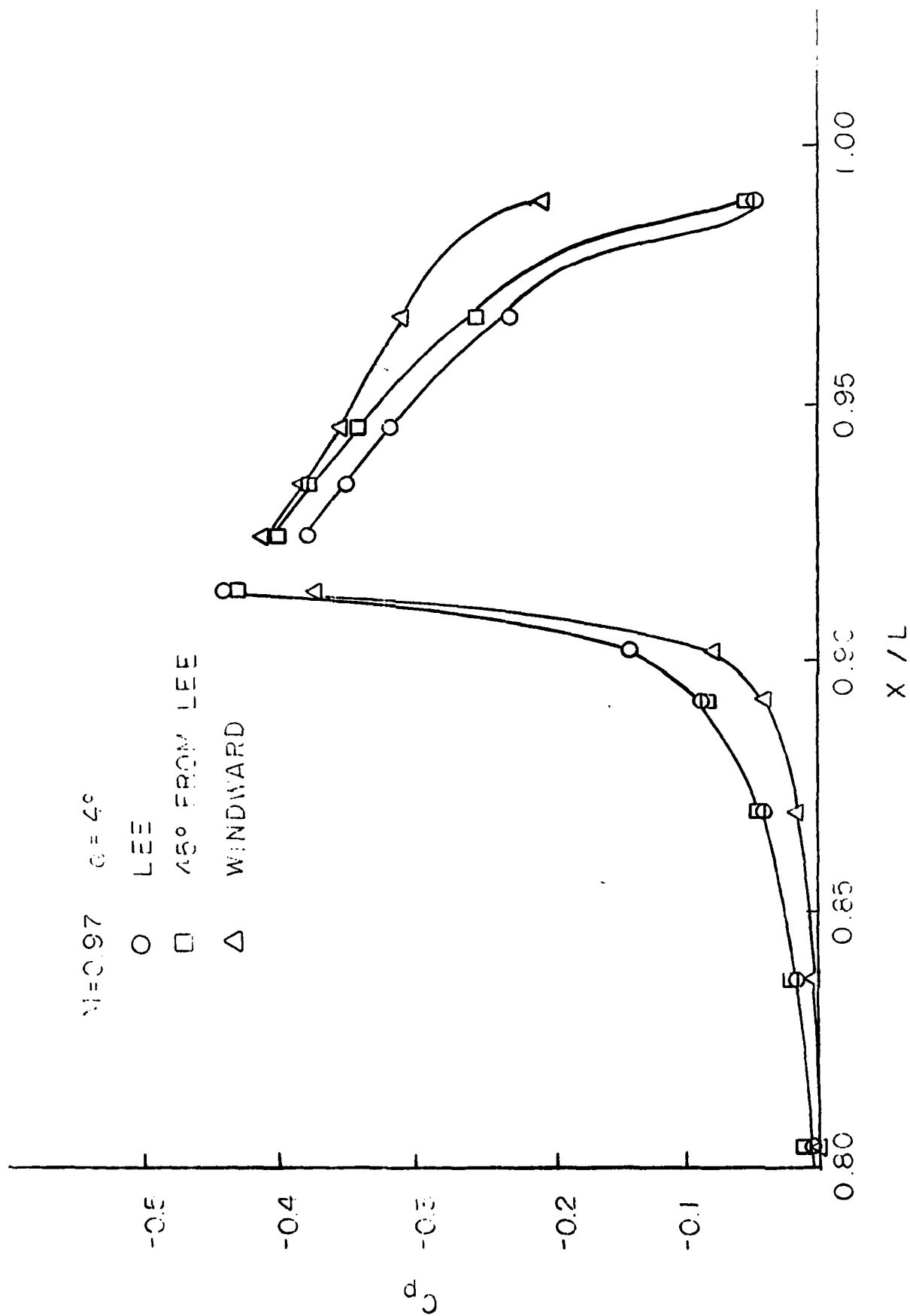


Fig. 31 Pressure coefficient distribution on conical boattail, $\alpha = 4^\circ$, $M_\infty = 0.97$.

gitudinal pressure distributions were obtained every 45° in circumferential angles around the model.

Boattail Drag

The pressures on the boattail have been numerically integrated to determine the boattail drag for the 7° conical afterbody as well as that for the triangular boattail. Figure 32 compares the incremental drag coefficient for the triangular model with that of a 1.0¹⁶ and the 0.5 caliber conical boattail. At a Mach number of $M_\infty = 0.94$ the triangular shape is seen to have only 48% of the drag of the conventional conical boattail. Very little difference between the 1.0 and the 0.5 caliber boattail is observed here as might be expected in light of the pressures rapid rise to nearly ambient pressure ($C_p \approx 0$) downstream of the shock wave as shown in Figure 27. Thus little additional drag is incurred because of the longer boattail.

As pointed out earlier, the base drag can be assumed approximately the same for triangular and conical shaped afterbodies if the base areas are the same. The models used in these tests had slightly different base areas with the triangular model 83.4% of the conical. However, it was not possible to measure base pressures accurately in the present case because of the relatively large sting required to support the heavy model. Base pressures were observed to be considerably higher than would be predicted by available correlations of free-flight data.¹⁷

Estimates of the total free-flight drag for the conical model gives the following components ($M_\infty = 0.94$, $\alpha = 0^\circ$, 1/2 = caliber 7° boattail)

$$\begin{aligned}\Delta C_{D \text{ Nose}} &= 0.019 \text{ (ref. (16))} \\ \Delta C_{D \text{ Boattail}} &= 0.077 \text{ (present tests)} \\ \Delta C_{D \text{ Base}} &= 0.152 \text{ (ref. (17))} \\ C_{D \text{ Total}} &= 0.248\end{aligned}$$

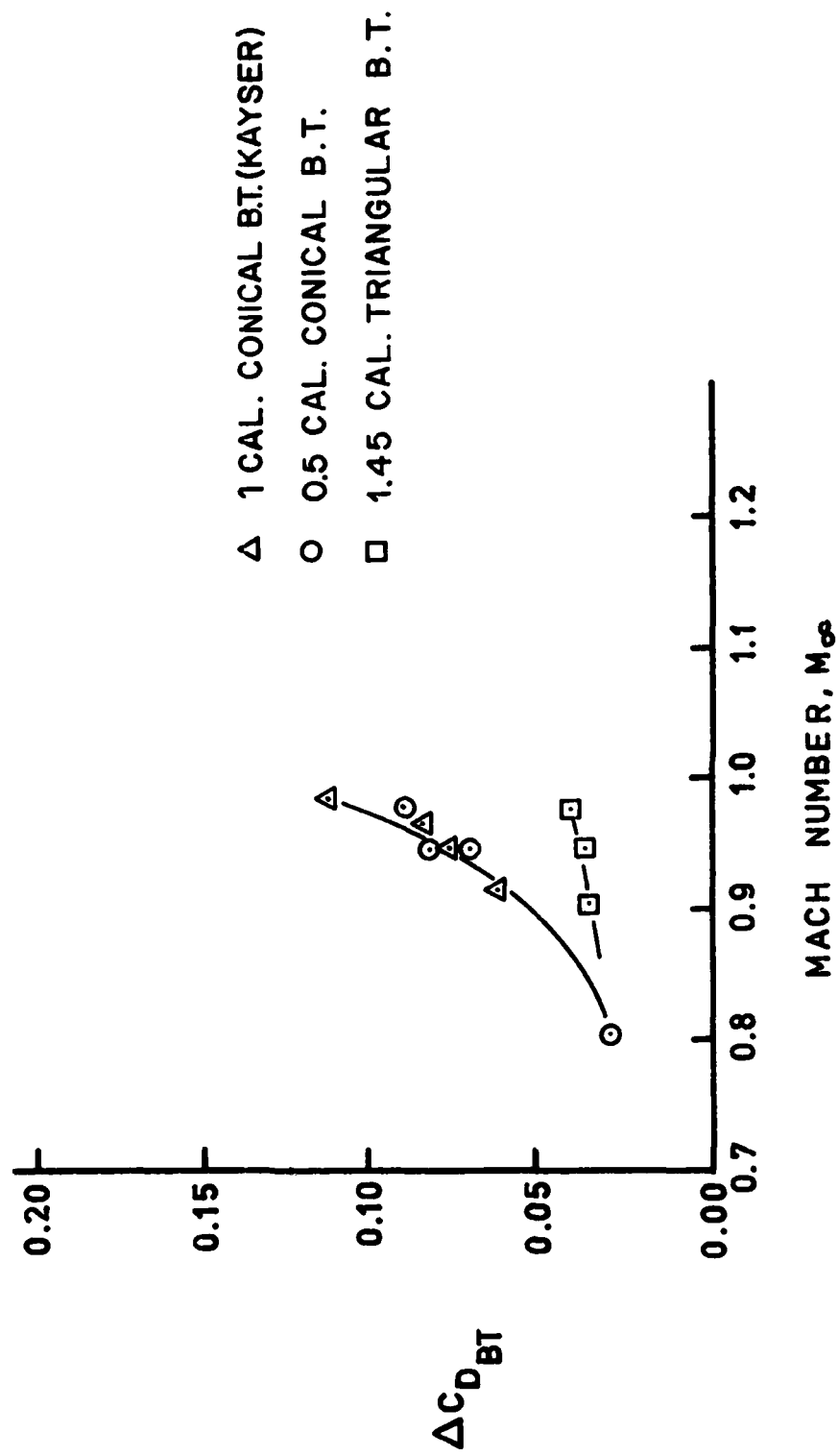


Figure 32. Boattail contribution to the drag coefficient for a conical and triangular configuration

Thus a 48% reduction in the boattail component results in a 15.5% reduction in overall drag. In conclusion then, these data and estimates show a significant improvement in drag performance for the triangular boattail.

Pitching Moment

The contribution of the boattail to the static stability in pitch has been evaluated for three configurations (cylindrical, conical and triangular) based on the pressure distribution data already discussed. The center of gravity location was assumed at 60% of the model length from the nose. The surface pressure distributions were integrated circumferentially to determine the longitudinal rate of change of the moment coefficient using the following equation:

$$\frac{dC_M}{dx/L} = \frac{4}{\pi} \left(\frac{L}{D}\right)^2 \left(\frac{x}{L} - 0.6\right) \oint c_p \bar{n} \cdot \bar{j} dS/D$$

where $\bar{n} \cdot \bar{j}$ = the cosine of the angle between the local surface normal and the lee side. The integration extended completely around the circumference S . The small difference between surface slant height and the longitudinal coordinate is neglected in these calculations. Figures 33-35 show the resulting $dC_M/d(x/L)$ distributions calculated for the last 25% of the model for a cylindrical, 7° conical and triangular afterbody. All these calculations are for $M_\infty = 0.94$, $\alpha = 4^\circ$ and $L/D = 5.8$. The cylindrical afterbody shows $dC_M/d(x/L)$ to be negative in this region which implies a stabilizing contribution to the overall moment coefficient. The upstream effect of the expansion at the model base under the influence of the three-dimensional flow field at 4° angle of attack produced a significantly larger afterbody contribution in the last 10% of the model than over the more upstream cylindrical sections. Although the afterbody contri-

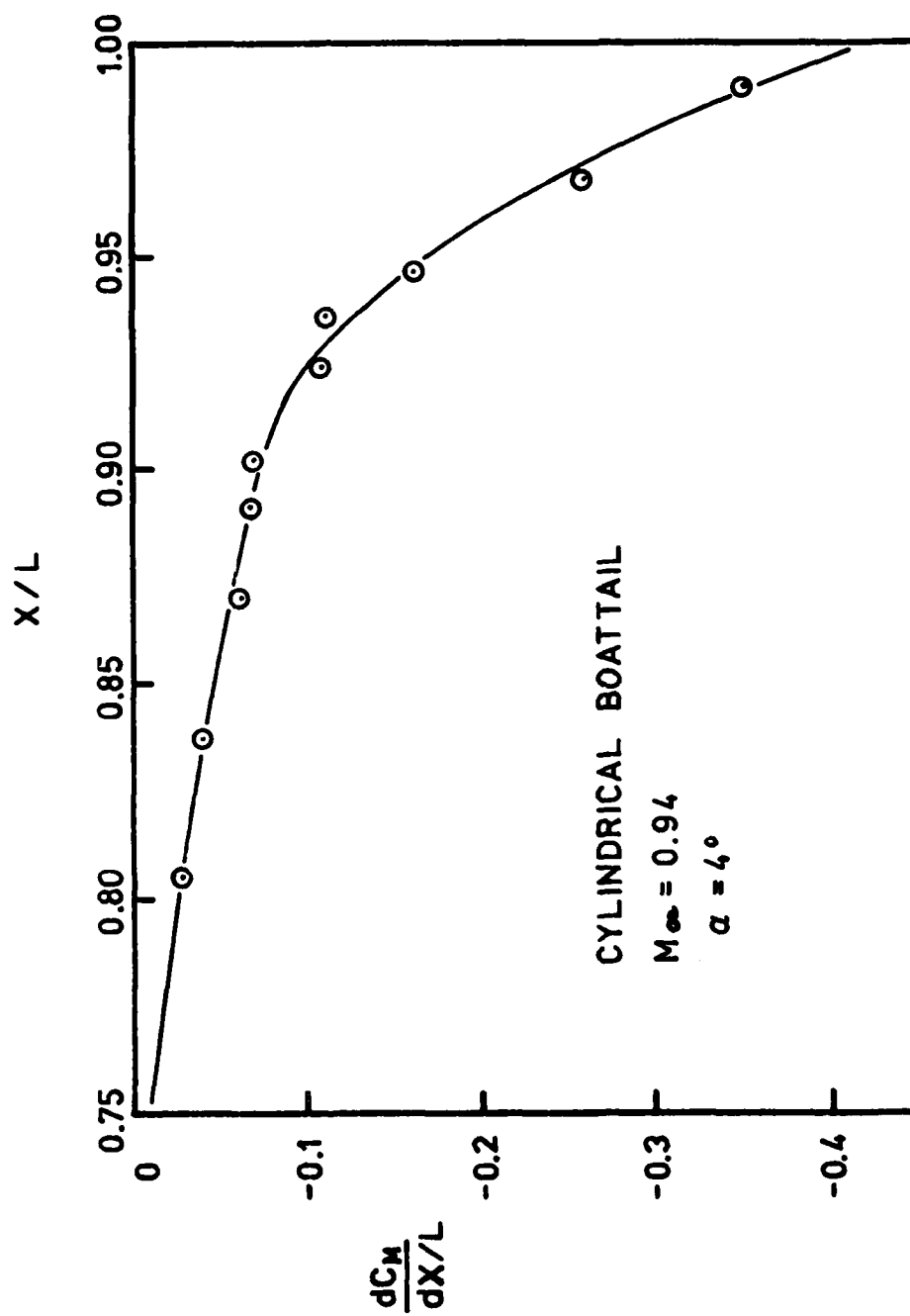


Figure 33. Afterbody contribution to the pitching moment coefficient - cylindrical afterbody ($M_\infty = 0.94$, $\alpha = 4^\circ$).

butes a stable moment it should be recognized that the nose and cylinder ahead of the center of gravity produce a destabilizing moment large enough to make the projectile statically unstable.

Figure 34 shows $dC_M/d(x/L)$ for the same x/L region on a 0.5 caliber, 7° conical boattail. The conical afterbody begins at $x/L = 0.913$. Upstream of that point we observe the effects of the expansion at the junction which produces a stabilizing contribution similar to the effect of the base on the cylindrical afterbody. In the expansion region on the boattail there is a strong destabilizing contribution. This can be viewed as being caused by the recompression shock wave which terminates the supersonic flow created by the expansion. At these transonic Mach numbers the shock wave is essentially plane and normal to the free-stream flow; thus its axial position varies around the body being more forward on the lee side and the reverse on the windward side. The effect on the model pressure distribution can be seen in Figures 30 and 31. The destabilizing contribution of the boattail is significantly larger than the stabilizing effect on the cylindrical section, resulting in a substantially more unstable projectile. The data summarized by Platou in Figure 26 shows about a 50% larger $C_{M\alpha}$ for the conical as compared to the cylindrical afterbody. L. Kayser has determined moment coefficient distribution for a slightly different configuration ($L/D = 6$, smaller scale, 1-caliber, 7° conical boattail) and he has found $\Delta C_{M \text{ Boattail}} = 0.075$ ($M_\infty = 0.94$, $\alpha = 4^\circ$) which is in good agreement with the value of $\Delta C_M = 0.079$ for the present 0.5 caliber conical boattail.

The results for the triangular boattail are shown in Figure 35. In this case the afterbody is 1.44 calibers or 25% of the 5.8 caliber long model. Integration of the pressure distribution is considerably more difficult because of the problem of defining the rather complicated circumferential pressure distributions with a finite number of pressure taps. The $x/L = 0.881$ station contained the highest density of taps and probably has the most accurate $dC_M/d(x/L)$ values. Because of the lack of model symmetry the moment contribution changes with orientation and three representative

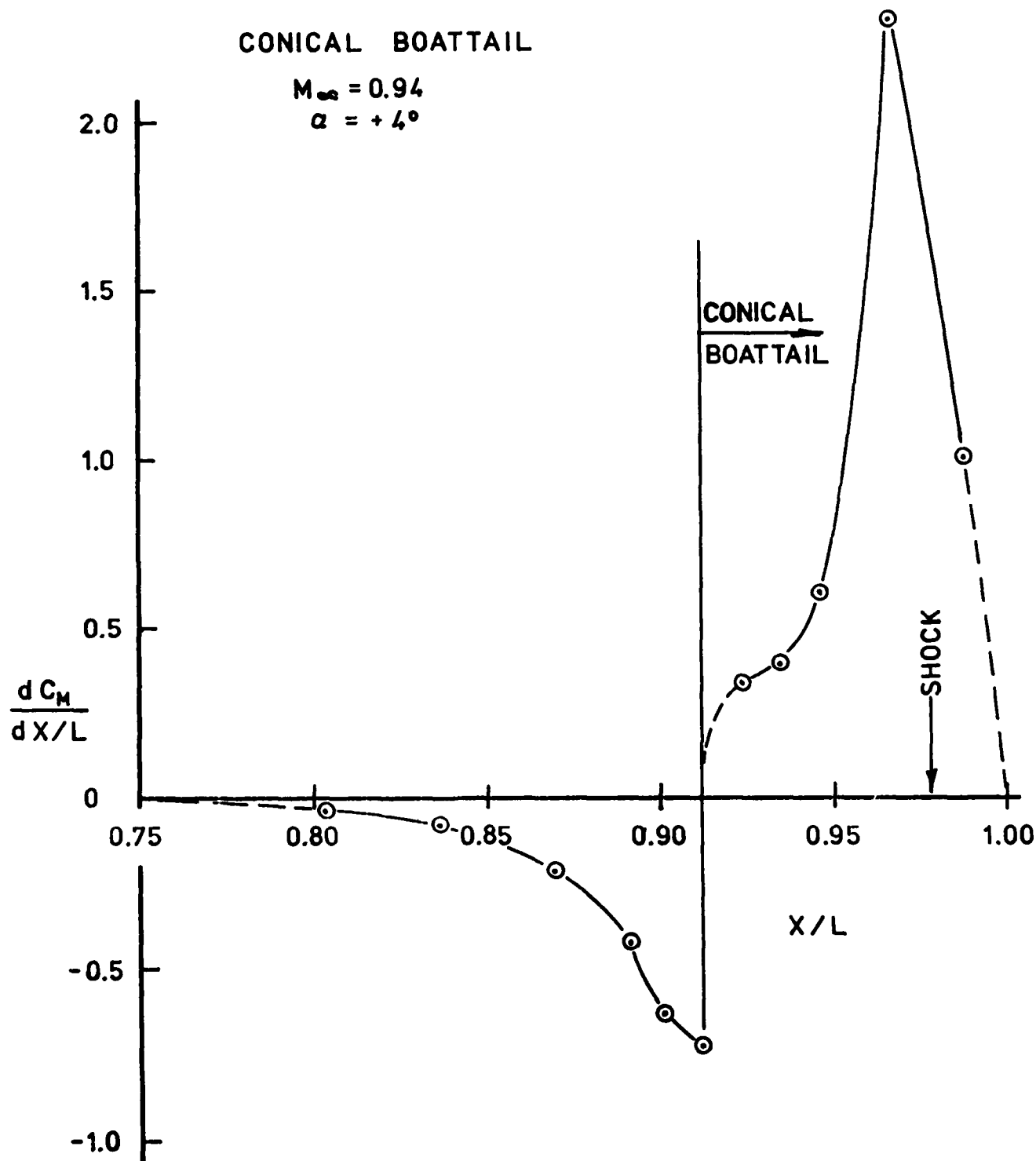


Figure 34. Afterbody contribution to the pitching moment coefficient - 7° conical boattail ($M_\infty = 0.94$, $\alpha = 4^\circ$).

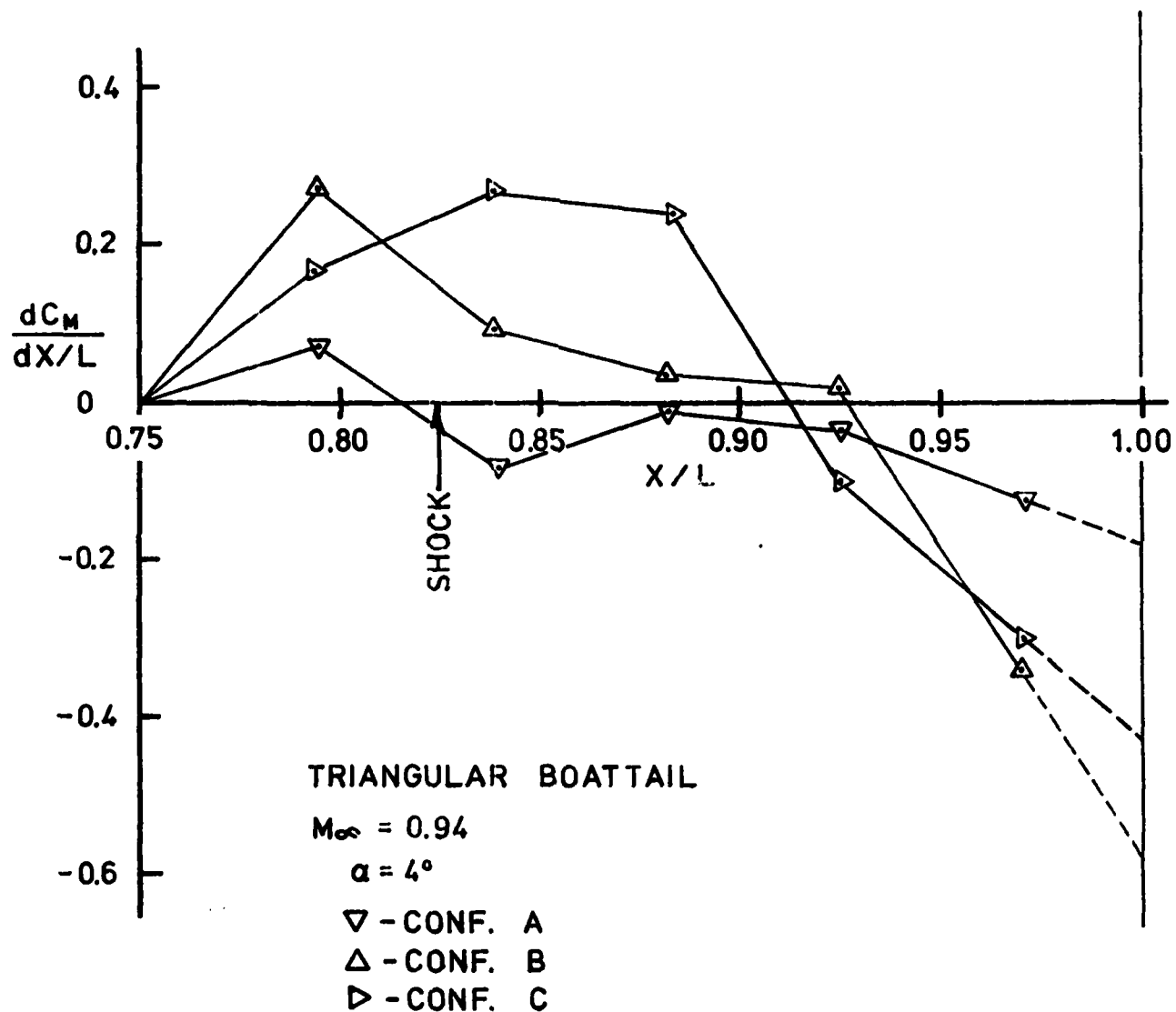


Figure 35. Afterbody contribution to the pitching moment coefficient - triangular boattail ($M_\infty = 0.94$, $\alpha = 4^\circ$).

situations are shown here. The orientation of the triangular symbol in the figure indicates the orientation of the model cross section relative to this cross flow velocity.

All these moment distribution data were integrated as a function of x/L for the last 25% of the projectile to obtain the C_M contributions which are compared in the following table.

TABLE 5

Afterbody	ΔC_M	ΔC_{M_α}
<u>Cylindrical</u> (1.44 Cal.)	-0.025	-0.36
<u>Conical</u>		
(0.5 Cal. 7° Conical 0.96 Cal. Cylinder)	+0.053	+0.76
<u>Triangular</u> (1.44 Cal.)		
Configuration A	-0.012	-0.16
" " B	+0.010	+0.14
" " C	+0.008	+0.11
<u>Average</u> (A+B)/4+C/2	+0.0035	+0.05

These data show that even in the most unfavorable orientation the triangular afterbody is more stable than the conventional conical configuration by a significant margin although not as stable as the high drag cylinder.

SUMMARY AND CONCLUSIONS

An effective reduction of artillery projectile drag is achieved by conically boattailing the afterbody where the primary effect is a reduction in the base area on which the low base pressure acts. The conical boattail also contributes to the overall drag because of the low pressures experienced downstream of the boattail-cylinder junction which can produce locally supersonic flow at transonic speeds. This supersonic flow is followed by a recompression shock wave whose location depends on the free stream Mach number. However, the shock wave and the viscous flow regions affected by the resulting pressure rise can produce significant destabilizing moments on a projectile at angle of attack which can degrade the shell performance to the extent of making it useless at transonic speeds.

In an attempt to improve the aerodynamics of projectiles at transonic speeds new afterbody configurations other than the conical boattail are being investigated. One promising configuration is the triangular afterbody in which the basic cylindrical shell is tapered by three planes which reduce the cylinder to an inscribed equilateral triangle. Ballistic range and force balance wind tunnel tests indicate such a configuration can reduce the drag and moderate the pitching moment peak in the transonic speed range. In order to more fully understand how these beneficial effects were produced, a wind tunnel investigation was initiated to measure in some detail the pressure distribution and the viscous flow characteristics on a triangular afterbody model.

A 5.8 caliber long model with a 3.2 caliber ogive nose, 1.16 caliber cylinder and 1.44 caliber triangular afterbody was used to obtain pressure distributions and boundary profiles at transonic speeds. These tests were made in the transonic pressure tunnel at NASA Langley Research Center at Mach numbers 0.90, 0.94, and 0.97 and at 0 and 4 degrees angle of attack. The model incorporated an internally mounted probe mechanism which was used to measure the properties of the Mach number 0.94 boundary layer on the after-

body at several longitudinal and circumferential stations.

The pressure distribution measurements showed that there was relatively little circumferential variation except for low pressure peaks which were observed near the cylinder-flat surface junction. The lowest pressures occurred at the most forward point on the flat. At the beginning of the afterbody, the lower pressure spike is followed by a rapid recompression not directly related to the subsequent shock wave. This pressure adjustment is more rapid than in the conical boattail case. In the $M_\infty = 0.97$ case and to a lesser extent in the 0.94 measurement the pressure tended to level out ahead of the shock wave and then rapidly increase again in the vicinity of where the shock wave was observed in Schlieren pictures.

If a triangular afterbody is assumed to have the same base drag as a conical boattail when the base to maximum cross sectional area ratio is the same, then the triangular afterbody is about 64% longer than the conical body. In that case the afterbody drag contribution at $M_\infty = 0.94$ is approximately 50% of that of the conical configuration based on integration of the measured pressure distributions.

The pressure distribution data also permit evaluation of the pitching moment contribution of different afterbodies. A simple cylindrical afterbody configuration is optimum from a stability point of view since the upstream effect of the expansion at the base creates a negative or stabilizing contribution to the overall moment. A simple conical boattail produces a similar favorable effect in the region ahead of the actual boattail because of the upstream effect of the expansion corner. However the subsequent shock wave when it occurs on the boattail produces an overriding destabilizing moment. This positive moment is created because the shock wave is basically normal to the free stream flow even when the projectile is at an angle of attack. Thus the high pressure behind the wave is more forward on the lee side of the body than on the windward side. The sharp pressure change across the

shock is, of course, spread out because of the intervention of the boundary layer but the overall pressure level is higher on the boattail lee side.

The same general picture of the flow applies to the non-conical afterbody as well except that the magnitude of the positive pitching contribution is significantly less than that of the conical shape. The more rapid pressure increase after the start of the afterbody independent of the shock wave position is a factor in reducing the upstream effect of the shock induced pressure rise. Another general factor is the considerably longer afterbody in the triangular case which results in a smaller moment arm to the center of gravity and that the favorable effect of the expansion at the base as on a cylinder also occurs. This latter effect may be expected to be observed on a longer conical boattail than the 0.5 caliber used in the present tests. The moment contribution of the orientation of the unsymmetric cross sectional shape.

In order to efficiently measure the distribution of boundary layer properties a three probe rake was initially employed which permitted surveying at three circumferential location at one time. However, the size of the mechanism required proved to cause significant static pressure variation on the model surface as compared to pressure measurements made without the mechanism installed. A smaller single probe mechanism was employed to duplicate and extend the rake data where the surface pressure interference effects were substantially reduced, although not eliminated. Comparison of the boundary layer properties determined by both methods showed little or no differences. The boundary layer thicknesses measured were strongly correlated with the wall static pressure distribution being smallest near the cylinder-flat junctions and thickest on the centerline of the flat and on the lee side at angle of attack. The shape of the profile is consistent with fully turbulent attached viscous flow in which the displacement thickness gradients produce relatively little effect on the pressure distribution except possibly in the immediate vicinity of the corner expansions and the shock waves.

REFERENCES

1. Platou, A. S., "An Improved Projectile Boattail," AIAA Paper No. 74-779, AIAA Mechanics and Control of Flight Conference, 1974.
2. Platou, A. S., "An Improved Projectile Boattail," BRL Memorandum Report No. 2395, U. S. Army Ballistic Research Laboratories, Aberdeen Proving Ground, MD, 1974.
3. Platou, A. S., "An Improved Projectile Boattail, Part II," BRL Report No. 1866, U. S. Army Ballistic Research Laboratories, Aberdeen Proving Ground, MD, 1976.
4. Platou, A. S., "An Improved Projectile Boattail, Part III," BRL Memorandum Report No. 2644, U. S. Army Ballistic Research Laboratories, Aberdeen Proving Ground, MD, 1976.
5. Platou, A. S., "Yawsonde Flights of 155 MM Non-Conical Boat-tail Projectiles and the 155 MM M549 Projectile at Tonopah Test Range - October 1977," BRL Memorandum Report ARB2L-MR-02881, U. S. Army Armament Research and Development Command, Ballistic Research Laboratory, Aberdeen Proving Ground, MD, 1978.
6. Platou, A. S., "Yawsonde Flights of 155 MM Non-Conical Boat-tail Projectile-B Configurations at Tonopah Test Range - March 1978," U. S. Army Ballistic Research Laboratory ARADCOM Memorandum Report ARBRL-MR-02908, Aberdeen Proving Ground, MD, 1979.
7. Deiwert, G. S., "Numerical Simulation of Three-Dimensional Boattail Afterbody Flow Fields," AIAA Journal 19, 5, pp. 582-588, 1981.
8. Reubush, D. E., "Experimental Study of the Effectiveness of Cylindrical Plume Simulators for Predicting Jet-On Boattail Drag at Mach Numbers up to 1.30," NASA TN D-7795, 1974.
9. Benek, J. A., "Separated and Non-Separated Turbulent Flows About Axisymmetric Nozzle Afterbodies, Part I, Detailed Surface Measurement," AEDC-TR-78-49; Part II, Detailed Flow Measurement," AEDC-TR-79-22, October 1979.
10. Shrewsbury, G. D., "Effect of Boattail Junction Shape on Pressure Drag Coefficients of Isolated Afterbodies," NASA TNX-1517, 1968.
11. Pulliam, T. H. and Steger, J. L., "On Implicit Finite Difference Simulation of Three Dimensional Flow," AIAA Journal 18, 2, pp. 159-167, 1980.

12. Scheff, L. B. and Steger, J. L., "Numerical Solution of Steady Supersonic Viscous Flow," AIAA Paper No. 79-130, New Orleans, LA, 1979.
13. Danberg, J. E., Reklis, R. P. and Inger, G. R., "Pressure Distributions and Boundary Layer Profiles on a Yawed Projectile at Transonic Speeds," Technical Report #226, Department of Mechanical and Aerospace Engineering, University of Delaware, Newark, DE, 1979.
14. Reklis, R. P., Danberg, J. E. and Inger, G. R., "Boundary Layer Flows on Transonic Projectiles," AIAA Paper No. 79-1551, AIAA 12th Fluid and Plasma Dynamics Conference, Williamsburg, VA, 1979.
15. Kayser, L. D. and Sturek, W. B., "Aerodynamics Performance of Projectiles with Axisymmetric and Non-Axisymmetric Boat-tails," Memorandum Report No. 03022, U. S. Army Armament Research and Development Command, Ballistic Research Laboratory, Aberdeen Proving Ground, MD, 1980.
16. Kayser, L. D., personal communication concerning data to be published, 1981.
17. McCoy, R. L., "'MC DRAG' - A Computer Program for Estimating the Drag Coefficients of Projectiles," Tech. Rpt. ARBRL-TR-02293, U. S. Army Armament Research and Development Command, Ballistic Research Laboratory, Aberdeen Proving Ground, MD, 1981.

DAT
ILMI